

Nested oscillatory dynamics in cortical organoids model early human brain network development

Cleber A. Trujillo^{1,2,*}, Richard Gao^{3,*}, Priscilla D. Negraes^{1,2,*},

Isaac A. Chaim², Alain Domissy², Matthieu Vandenberghe⁴, Anna Devor^{4,5}, Gene W. Yeo^{2,6,7},

Bradley Voytek^{3,8, ¶} & Alysson R. Muotri^{1,2,8,9, ¶}

¹University of California San Diego, School of Medicine, Department of Pediatrics/Rady Children's Hospital San Diego, La Jolla, California 92093, USA.

²University of California San Diego, School of Medicine, Department of Cellular & Molecular Medicine, La Jolla, California 92093, USA.

³University of California San Diego, Department of Cognitive Science, Neurosciences Graduate Program, Institute for Neural Computation, La Jolla, California 92093, USA.

⁴University of California San Diego, Department of Radiology, Department of Neurosciences, La Jolla, California 92093, USA;

⁵Harvard Medical School, Massachusetts General Hospital, Martinos Center for Biomedical Imaging, Charlestown, MA 02129, USA.

⁶Molecular Engineering Laboratory, Agency for Science, Technology and Research, Singapore, Singapore.

⁷Department of Physiology, Yong Loo Lin School of Medicine, National University of Singapore, Singapore, Singapore.

⁸University of California San Diego, Kavli Institute for Brain and Mind, La Jolla, California 92093, USA.

⁹Center for Academic Research and Training in Anthropogeny (CARTA), La Jolla, California 92093, USA.

* These authors contributed equally to this work.

¶ Correspondence to:

Dr. Muotri, 2880 Torrey Pines Scenic Drive, La Jolla, CA 92093. MC0695, Email: muotri@ucsd.edu, or

Dr. Voytek, 9500 Gilman Drive, La Jolla, CA 92093. MC0515, Email: bvoytek@ucsd.edu.

SUMMARY

Structural and transcriptional changes during early brain maturation follow fixed developmental programs defined by genetics. However, whether this is true for functional network activity remains unknown, primarily due to experimental inaccessibility of the initial stages of the living human brain. Here, we analyzed cortical organoids that spontaneously developed periodic and regular oscillatory network events that are dependent on glutamatergic and GABAergic signaling. These nested oscillations exhibit cross-frequency coupling, proposed to coordinate neuronal computation and communication. As evidence of potential network maturation, oscillatory activity subsequently transitioned to more spatiotemporally irregular patterns, capturing features observed in preterm human electroencephalography (EEG). These results show that the development of structured network activity in the human neocortex may follow stable genetic programming, even in the absence of external or subcortical inputs. Our model provides novel opportunities for investigating and manipulating the role of network activity in the developing human cortex.

KEYWORDS: brain organoids, network oscillations, stem cells, phase-amplitude coupling, preterm electroencephalography, Methyl-CpG-binding protein 2 (MECP2).

HIGHLIGHTS

- Early development of human functional neural networks and oscillatory activity can be modeled *in vitro*.
- Cortical organoids exhibit phase-amplitude coupling between delta oscillation (2 Hz) and high-frequency activity (100-400 Hz) during network-synchronous events.
- Differential role of glutamate and GABA in initiating and maintaining oscillatory network activity.
- Developmental impairment of MECP2-KO cortical organoids impacts the emergence of oscillatory activity.
- Cortical organoid network electrophysiological signatures are similar to human preterm neonatal EEG features.

IN BRIEF

Brain oscillations are a candidate mechanism for how neural populations are temporally organized to instantiate cognition and behavior. Cortical organoids initially exhibit periodic and highly regular nested oscillatory network events that eventually transition to more spatiotemporally complex activity, mimicking features of late-stage preterm infant electroencephalography. Functional neural circuitry in cortical organoids exhibits emergence and development of oscillatory network dynamics similar to features found in the developing human brain.

1 INTRODUCTION

2 Diverse and hierarchical cellular networks develop into circuits with patterns of functional
3 spatiotemporal activity to form the human brain. Neural oscillations, a prominent, rhythmic brain
4 signal found across species, robustly track cognitive, behavioral, and disease states (Buzsáki and
5 Draguhn, 2004; Fries, 2005; de Hemptinne et al., 2015; Henriques and Davidson, 1991; Khan et
6 al., 2013; Uhlhaas and Singer, 2010) and have long been leveraged in cognitive and systems
7 neuroscience due to their ubiquity and accessibility. These complex network dynamics emerge
8 early in development, and is unclear if shaped exclusively by biological programming prenatally
9 (Blankenship and Feller, 2010; Johnson, 2001; Power et al., 2010). *In vitro* and *in vivo* rodent
10 studies have shown that a conserved repertoire of organized network activity, such as traveling
11 waves, giant depolarizing potentials, and early network oscillations, develop according to a
12 consistent timeline prior to and immediately after birth (Allene et al., 2008; Khazipov and
13 Luhmann, 2006; Uhlhaas et al., 2010). However, due to an inability to interrogate the
14 electrophysiology of intact embryonic brains, it remains unknown whether the same happens in
15 humans. As a result, our knowledge about human brain functional development rests upon
16 extrapolations from nonhuman model systems (Power et al., 2010).

17 Organoids generated from induced pluripotent stem cells (iPSC) have emerged as a
18 scaled-down and three-dimensional model of the human brain, mimicking various developmental
19 features at the cellular and molecular levels (Camp et al., 2015; Lancaster and Knoblich, 2014;
20 Lancaster et al., 2013; van de Leemput et al., 2014; Luo et al., 2016; Mariani et al., 2012; Paşca
21 et al., 2015; Qian et al., 2016; Renner et al., 2017). Despite recent advances in the understanding
22 of their vast cellular diversity, there is no evidence that these organoids show complex and
23 functional neural network activity that resembles early human brain formation (Birey et al., 2017;
24 Quadrato et al., 2017). Therefore, researchers have not yet clearly determined whether organoids
25 are a suitable model for neural network dynamics (Kelava and Lancaster, 2016; Paşca, 2018).

26 Here, we use human iPSCs to generate cortical organoids that exhibit evolving and nested

27 oscillatory network dynamics over the span of several months. We subsequently investigated the
28 molecular basis of human brain oscillatory activity formation, maintenance, and temporal control
29 by gene targeting. Finally, we applied unsupervised machine learning to evaluate the similarity
30 between electrophysiological activity patterns of the *in vitro* model and human preterm neonatal
31 electroencephalogram (EEG). Our findings suggest that organoid models are suitable for the
32 investigation of the physiological basis of network formation at early and late stages of the human
33 brain development. This prolonged evaluation of cortical organoid activity expands our
34 understanding of the emergence of network-level neurodynamics in humans.

35

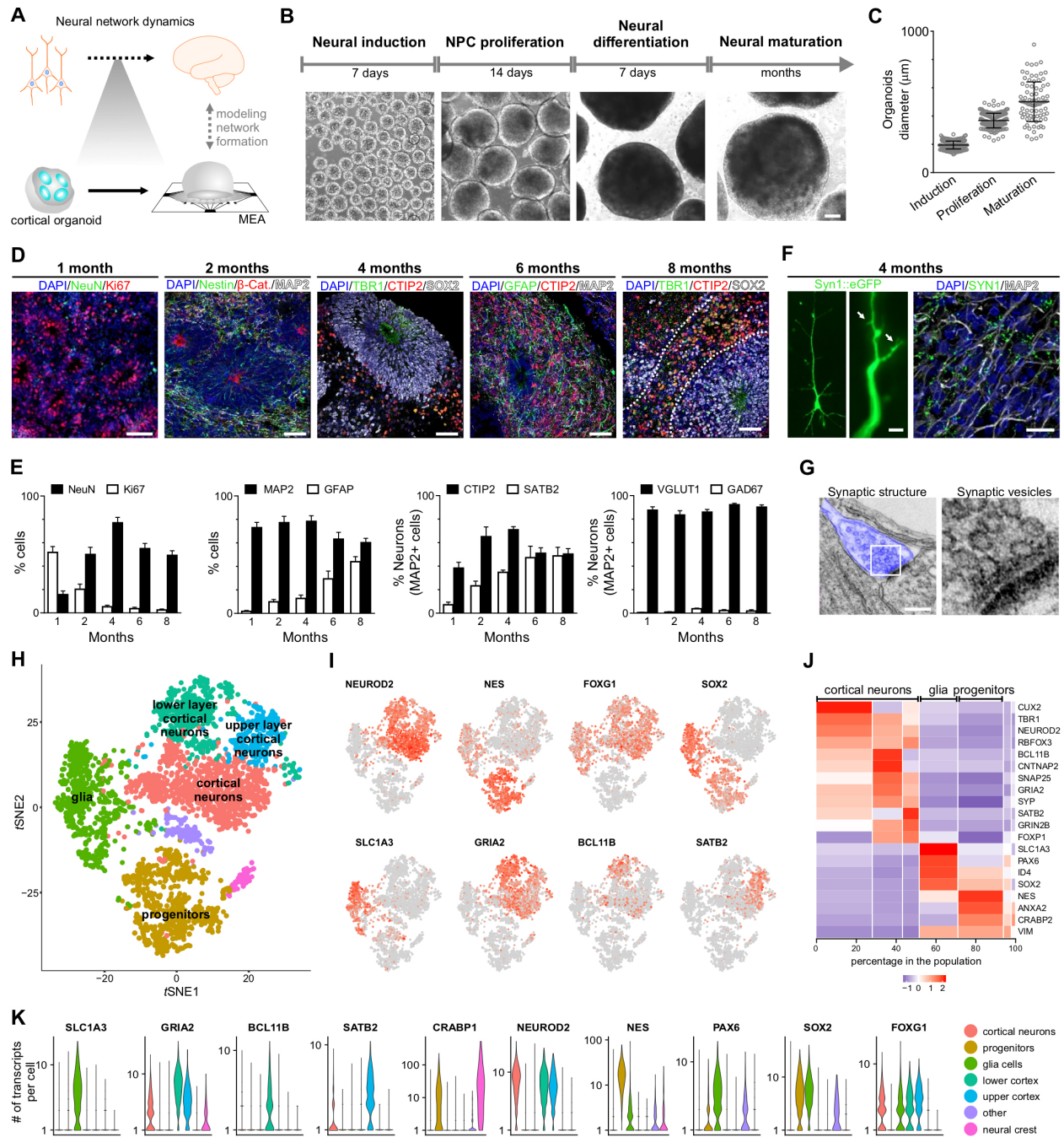
36 **RESULTS**

37 **Development of functional cortical organoids**

38 Despite the structural and transcriptional similarities between brain organoids and the
39 developing nervous system, the emergence of higher-level complex network activity comparable
40 to the living human brain remains largely untested (Figure 1A). To investigate the formation of a
41 functional network, we promoted cortical specification by modifying previously described
42 protocols (Paşca *et al.*, 2015; Thomas *et al.*, 2016) (Figure 1B, see Methods for details). At the
43 beginning of differentiation, an abundance of proliferative neural progenitor cells (NPCs) (Ki67+,
44 SOX2+ and Nestin+) that self-organized into a polarized neuroepithelium-like structure was
45 observed. Similar to human cortical development *in vivo*, the proliferative zone around a lumen
46 delimited by β -catenin+ cells was surrounded by progenitor cells. Progressively, the organoids
47 increased in size and in the proportion of mature neurons (NeuN+ and MAP2+) to ultimately
48 develop into concentric multi-layer structures composed of NPCs, intermediate progenitors
49 (TBR2+, also known as EOMES), and lower (CTIP2+, also known as BCL11B) and upper
50 (SATB2+) cortical layer neurons (Figure 1B-E and S1A-C). Although the initial fraction of glial
51 cells was less than 5%, this population increased to about 30-40% after 6 months of differentiation
52 (Figure 1D, 1E and S1D-H). The maturation level of the cells is reflected by the presence of

53 pyramidally-shaped neurons and formation of dendritic spine-like protrusions and synaptic
54 structures (Figure 1F and 1G).

55 To further characterize the cellular diversity of a cortical organoid, we performed single-
56 cell gene expression profiling in 6-month-old organoids and used unbiased clustering to classify
57 the main existing cell types. From two independent differentiation replicates (Figure S2), seven
58 distinct clusters were characterized based on their differential gene expression patterns (Figure
59 S3, S4 and Table S1) including: progenitors, glia, and cortical neurons, which could be further
60 subdivided into lower and upper layer based on the expression of the layer-specific markers
61 CTIP2 and SATB2, respectively (Figure 1H-K and Figure S1).



62

63 **Figure 1. Cellular and molecular development of human cortical organoids.** (A) Overview of
 64 human neural network formation and dynamics evaluation using organoids. (B) Schematic of the
 65 protocol used to generate cortical organoids. Scale bar, 200 µm. (C) Organoid growth during
 66 different developmental stages. (D) Representative immunostainings showing proliferating NPCs
 67 (Ki67+ and Nestin+), lower (TBR1+ and CTIP2+) and upper (SATB2+) cortical layer neurons and

68 glial cells (GFAP+) overtime. Scale bar, 50 μm . (E) Population analysis of specific markers
69 indicating stages of maturation and multiple neuronal subtypes. The data are shown as mean \pm
70 s.e.m. ($n = 8$). (F) Representative image of a pyramidal neuron (left panel); dendritic spine-like
71 structures (arrow) are observed in cells transduced with the SYN:EGFP reporter (middle panel;
72 scale bar, 5 μm). Immunohistochemical detection of the synaptic protein Syn1 (right panel; scale
73 bar, 50 μm). (G) Electron microscopy of synaptic structures in 4-month-old cortical organoids
74 (blue). (H) t -distributed stochastic neighbor embedding (t SNE) plot of 3,491 cells from 6-month-
75 old organoids. Colors denote seven main cell clusters. (I) t SNE plots depicting cell-type specific
76 marker expression levels (red denotes higher expression). (J) Heatmap of average expression
77 for representative gene markers by cluster and cell-type (see also Figure S4). (K) Violin plots
78 showing transcript levels for representative markers of each cluster (see Figure S3 for additional
79 markers).

80

81 **Emergence of nested oscillatory network activity**

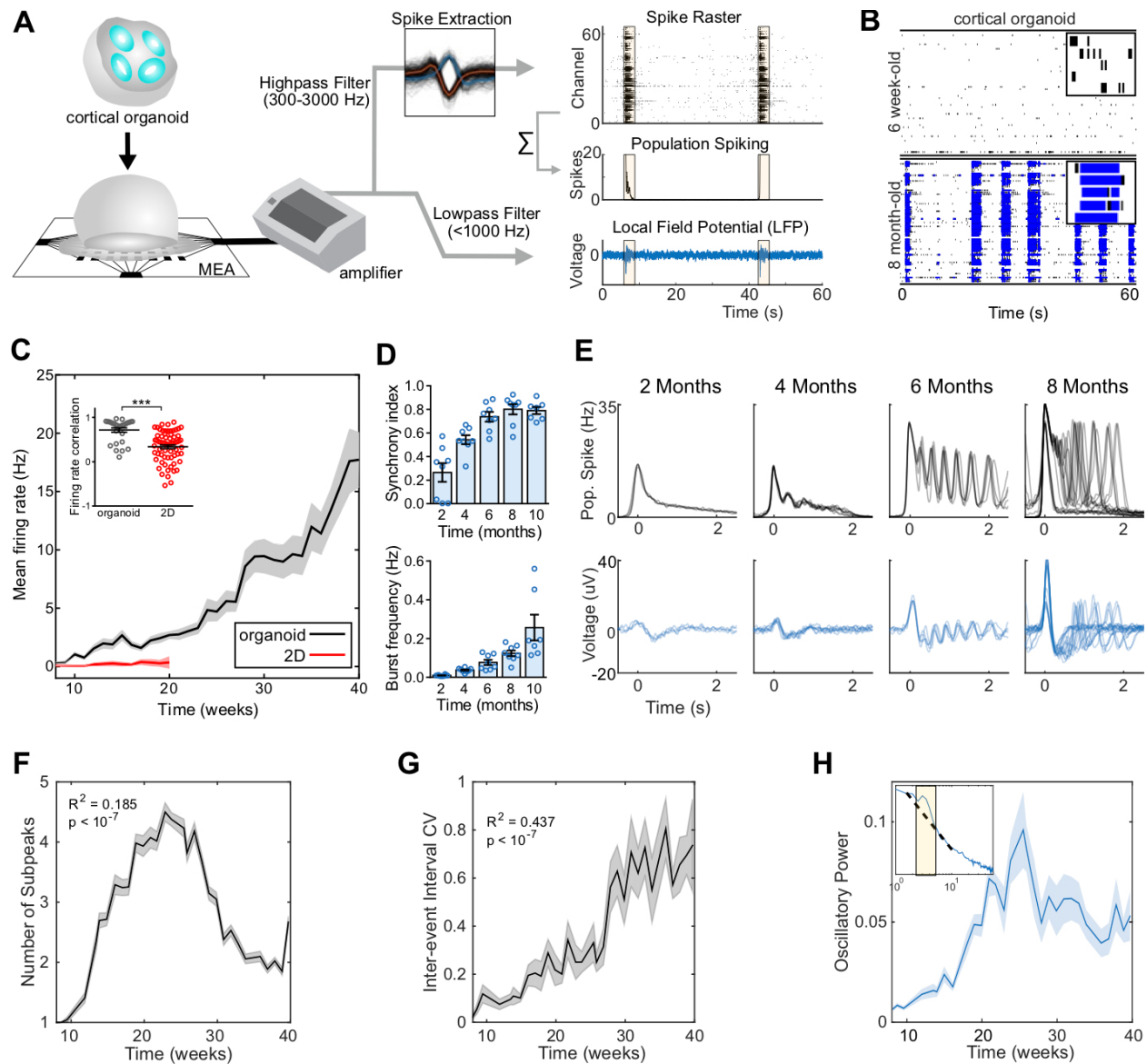
82 Considering the observed cellular diversity and expression of synaptic markers, we further
83 interrogated the presence of functional network activity. We performed weekly extracellular
84 recordings of spontaneous electrical activity using multi-electrode arrays (MEA). We separately
85 analyzed single-channel and population firing characteristics derived from channel-wise spike
86 times, and the local field potential (LFP); a measure of aggregate synaptic currents and other
87 slow ionic exchanges (Buzsáki *et al.*, 2012) (Figure 2A). The spikes from each channel do not
88 represent putative single-unit action potentials. Since the spatial resolution of MEA electrodes
89 was sparse, the total population spiking of a well was submitted for further analysis, rather than
90 individual spike trains. Over the course of 10 months, organoids exhibited consistent increases in
91 electrical activity, as parametrized by channel-wise firing rate, burst frequency, and spike
92 synchrony (Chen *et al.*, 2009; Lisman, 1997), which indicates a continually-maturing neural
93 network (Figure 2B-D and S5). Organoid firing rates were far higher than previously observed in

94 studies using iPSC-derived neurons or cerebral organoids (Figure S6). Additionally, the variability
95 between replicates over 40 weeks of differentiation was significantly lower compared to iPSC-
96 derived neurons in monolayer cultures (Figure 2C inset and S5E).

97 Population-level signals typically observed in *in vivo* electrophysiology were analyzed to
98 further probe the network properties of cortical organoids. During individual recordings, cultures
99 displayed a robust pattern of activity, switching between long periods of quiescence and short
100 bursts of spontaneous network-synchronized spiking (hereafter referred to as “network events”).
101 These network events are periodic but infrequent early in development (~2 months), occurring
102 roughly every 20 seconds and decayed monotonically after the initial onset, similar to previously
103 reported network “oscillations” in primary cultures and organoids (Figure 2E). From 4-months
104 onwards, a secondary peak emerged 300-500 ms after the initial network activation, leading to
105 the presence of a nested fast oscillatory (2-3 Hz) pattern up to 6-months in culture (Figure 2F and
106 Figure S7). Notably, this robust fast timescale oscillation was not observed in 3D neurospheres,
107 suggesting that the spherical arrangement of neurons is insufficient for the emergence of nested
108 oscillations (Figure S8). The regular oscillatory activity during network events transitioned to
109 stronger, yet more variable, oscillations over time. To quantify this network complexity, we tracked
110 the regularity (coefficient of variation of inter-event intervals, CV) and the spatial and temporal
111 correlation between spontaneous network events. The inter-event interval CV consistently
112 increased over 10 months of differentiation (Figure 2G), from extremely regular latencies ($CV \cong$
113 0) at 2 months to irregular, Poisson-like ($CV \cong 1$) at 10 months. This indicates increased variability
114 between consecutive network events initiation. Additionally, spatial and temporal irregularity on a
115 shorter time-scale (within-event) also increased with development, suggesting a breakdown of
116 deterministic population dynamics from the onset of network events (Figure S7G).

117 Periodic oscillatory activity is often defined as a “bump” over the characteristic $1/f$
118 background noise in the power spectral density (PSD) of extracellular signals above-and-beyond
119 the aperiodic $1/f$ signal (Buzsáki *et al.*, 2013; Gao *et al.*, 2017). In organoid LFPs, we observed

120 both prominent oscillatory peaks in the low-frequency range (1-4 Hz) and in the aperiodic signal
121 characteristic of neural recordings (Ben-Ari, 2001; Voytek et al., 2015). The development of
122 oscillatory activity in cortical organoids over time was quantified by computing the PSD for each
123 LFP recording (Figure 2H, inset). Oscillatory power in the delta range (1-4 Hz) increased for up
124 to 24 weeks in culture, tapering off slightly in subsequent recordings and plateauing during the
125 last 10 weeks. This inverted-U trajectory reflects the network's initial acquisition of oscillatory
126 modes at steady frequencies and the dispersion of this regularity at later time points. The LFP
127 results reveal the development of the cortical organoid cultures across different network states:
128 from sparse activity with extreme rigidity and regularity, to one that acquires repetitive, perhaps
129 overly-regular oscillatory patterns (Voytek and Knight, 2015), until it finally reaches a stage of
130 higher spatiotemporal complexity and variability that is reminiscent of self-organized critical
131 networks (Tetzlaff et al., 2010) (Figure S7C-G).



132

133 **Figure 2. Oscillatory network dynamics in long-term cortical organoids.** (A) Schematic of

134 the organoid signal processing pipeline. Raw MEA data is analyzed as population spiking and

135 LFP separately. Synchronous network events are highlighted in yellow. (B) Raster plot of network

136 spiking activity after 1.5 and 6 months of maturation. A 3-s interval of activity over 5 channels is

137 shown in the upper right corners. (C) Cortical organoids show elevated and continuously

138 increasing mean firing rate compared to 2D monolayer neurons ($n = 8$ organoid cultures, and $n =$

139 12 for 2D neurons). Inset, correlation of the firing rate vector over 12 weeks of differentiation (from

140 8 to 20) between pairs of cultures showing reduced variability among organoid replicates. (D)

141 Temporal evolution of cortical organoid network activity. Detailed definitions and further
142 parameters are presented in Figure 5B and 5C. (E) Time series of population spiking and LFP
143 during network events in cortical organoid development. Each trace represents a single event
144 during the same recording session. (F) Oscillatory dynamics within network events develop
145 nonlinearly, following an inverted-U trajectory. (G) Increase of network variability dynamics
146 throughout development. (H) Oscillatory power increases up to the 25th week in culture and
147 plateaus at 30 weeks. Inset, Oscillatory power is calculated by fitting a straight line (dashed) over
148 the aperiodic portion of the PSD and taken as the height of narrow peaks rising above the linear
149 fit. The data shown in C, D, F, G and H are presented as mean \pm s.e.m. *P < 0.05, **P < 0.01,
150 ***P < 0.001, unpaired Student's *t*-test (C), quadratic (F) and linear (G) regression.

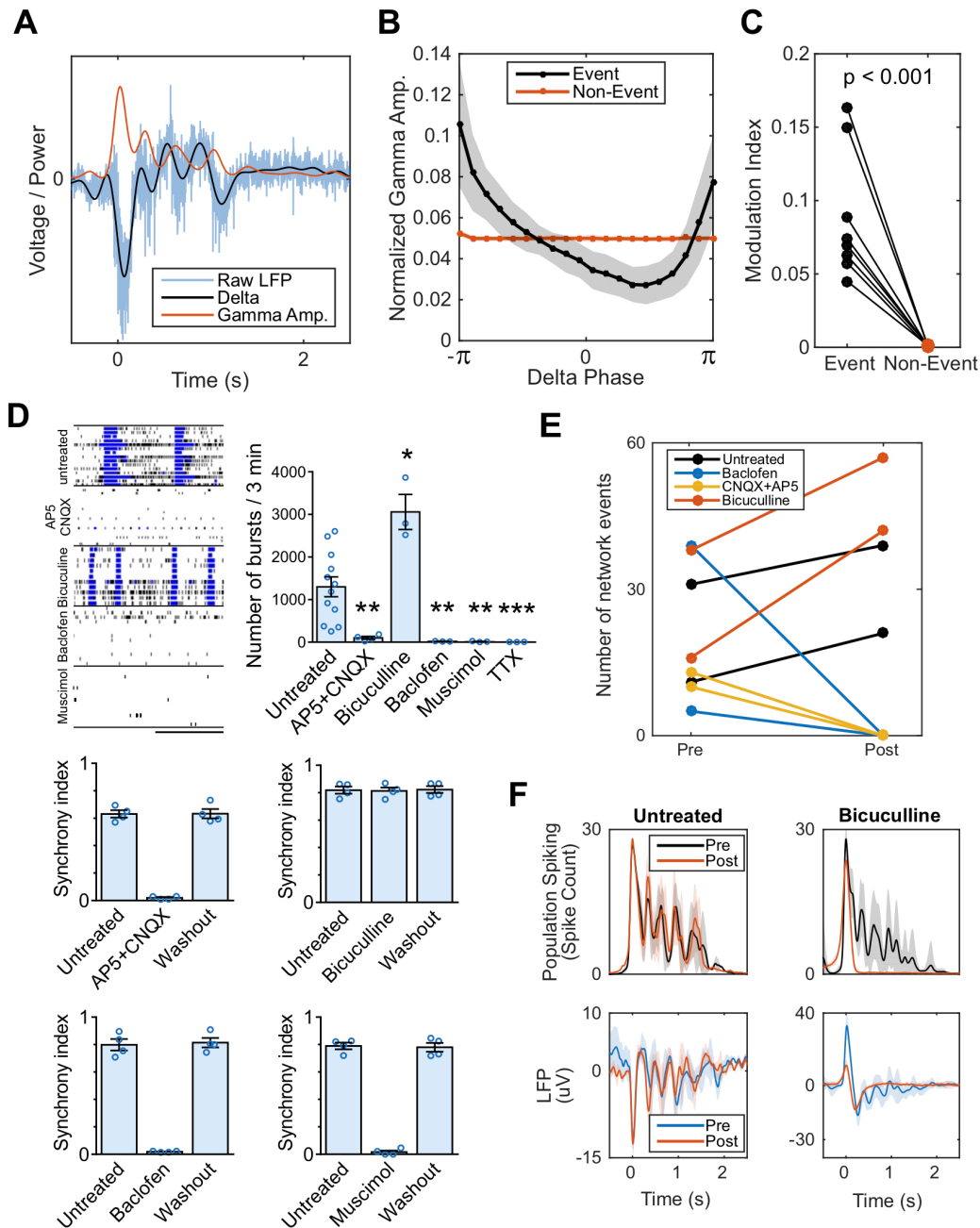
151

152 **Oscillatory coordination of neural ensembles and its synaptic mechanisms**

153 Oscillatory dynamics in the functioning brain have been postulated to coordinate spiking
154 across neural ensembles¹. In the LFP and other mesoscopic brain signals, this manifests as a
155 phenomenon known as cross-frequency phase-amplitude coupling (PAC) (Voytek and Knight,
156 2015), wherein the high-frequency content of the LFP is entrained to the phase of slow oscillations
157 (Manning *et al.*, 2009; Miller *et al.*, 2007; Mukamel *et al.*, 2005). PAC in the neocortex and
158 hippocampus has been shown to be functionally relevant in a range of behaviors and neurological
159 disorders (de Hemptinne *et al.*, 2015; Voytek and Knight, 2015; Voytek *et al.*, 2015). In the
160 organoids, we observed greater PAC between oscillatory delta (1-4 Hz) and broadband gamma
161 activity (100-400 Hz, see Methods) during network events compared to quiescent periods (Figure
162 3A-C). This result suggests that oscillations in the organoid may reproduce dynamics relevant for
163 the intact brain and could serve as a model to understand the fundamental mechanisms behind
164 the emergence of oscillatory networks in the developing human brain.

165 We further evaluated the role of glutamatergic and GABAergic synaptic transmission in
166 forming oscillations by pharmacological intervention. Organoid neural networks were susceptible

167 to both glutamate receptor antagonists (AP5 and CNQX; NMDA and AMPA/kainate, respectively)
168 and GABA receptor agonists (muscimol, GABA_A; baclofen, GABA_B) by significantly reducing the
169 number of spikes and bursts, with a subsequent extinction of synchronous activity. The electrical
170 activity was abolished in the presence of tetrodotoxin (TTX) (Figure 3D and 3E). Notably,
171 blockade of GABAergic transmission by bicuculline increased the number of network-
172 synchronized events and did not affect peak population firing rates, but abolished nested 2 Hz
173 oscillatory activity by erasing subsequent reverberant peaks (Figure 3F). The findings suggest
174 that GABA transmission is crucial for the maintenance, but not the initiation of faster oscillatory
175 activity. This is consistent with accounts of inhibition rhythmically coordinating pyramidal
176 populations activity during early development (Opitz et al., 2002).



177

178 **Figure 3. Cortical organoid serves as a model of functional oscillations and their synaptic**

179 **mechanisms.** (A-C) Phase-amplitude coupling is observed in organoid LFP during network

180 events, a phenomenon proposed to mediate neural communication *in vivo*. (A) Example of raw

181 LFP during a network event decomposed into its low-frequency component (1-4 Hz delta) and the

182 amplitude envelope of the high-frequency, broadband gamma component (200-400 Hz). Analysis

183 was repeated for 100-200 Hz with near identical effect size and significance. (B) Normalized

184 gamma amplitude binned by delta phase during network events (black) shows greater modulation
185 depth by low frequency delta than during non-event periods (red). (C) Phase-amplitude coupling
186 during network events is significantly greater than non-event periods in all batches. (D) Effect of
187 selective drug treatments on neuronal electrical activity in 6-month-old organoids. Representative
188 raster plots and burst measurements of untreated and treated organoids. Scale bar, 20 s.
189 Exposure to AP5 + CNQX, baclofen and muscimol reversibly extinguish the network bursts
190 (synchrony), while no changes were promoted by bicuculline. (E-F) Pharmacological perturbation
191 of oscillatory activity during network events in 6-month-old organoids. Application of bicuculline
192 increases the number of network events, while CNQX + AP5 and baclofen completely abolish
193 synchronized network events. Bicuculline blocks oscillatory network activity but not the network
194 event itself. Data are shown as mean \pm s.e.m.; unpaired Student's *t*-test.

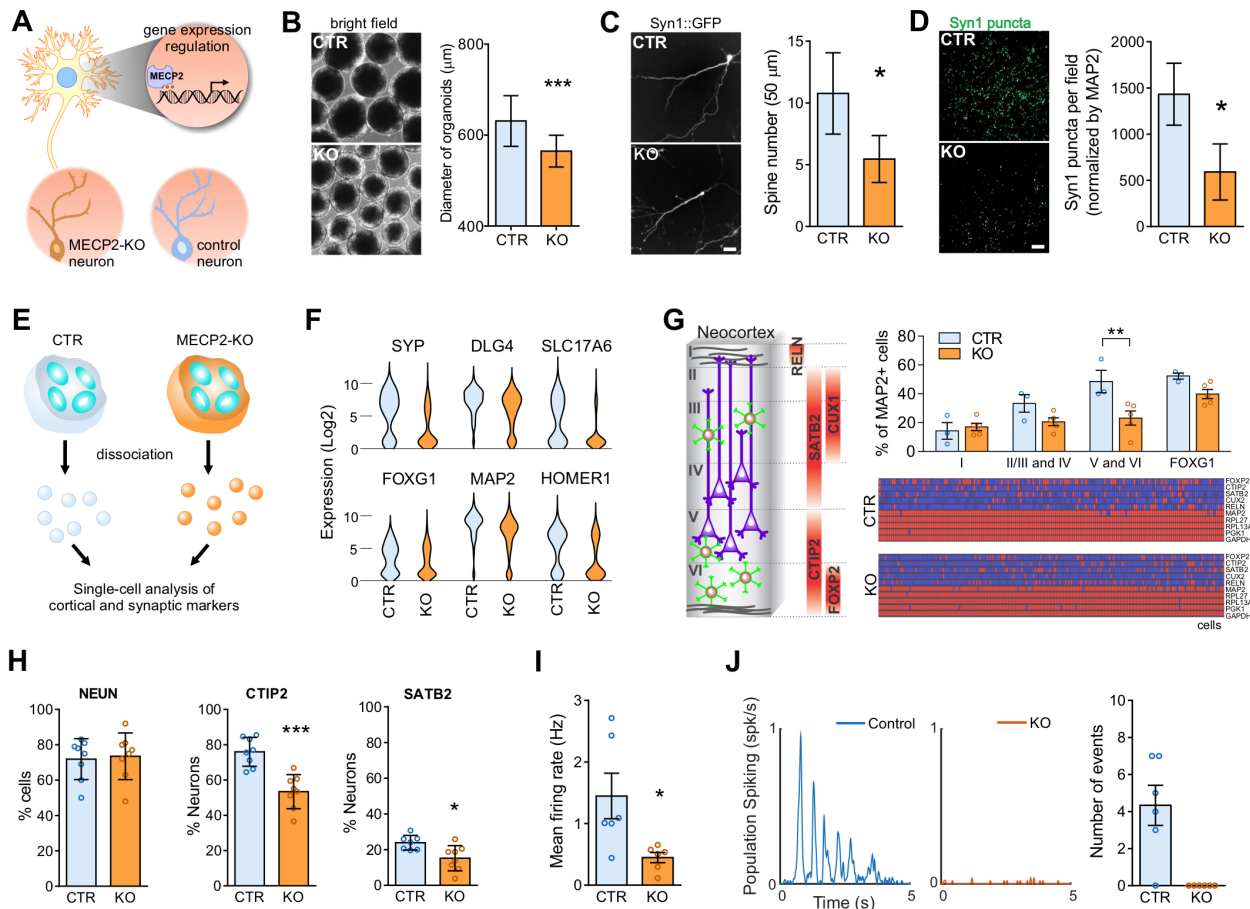
195

196 **MECP2 is essential for the timely emergence of network oscillations**

197 In addition to modeling the typically-developing brain, cortical organoids can also shed
198 light on the mechanism behind functional deficits in neurodevelopmental disorders (Birey *et al.*,
199 2017; Lancaster *et al.*, 2013; Thomas *et al.*, 2016). Normal oscillatory network dynamics in the
200 brain are often shown to break down in psychiatric and neurological conditions (Uhlhaas and
201 Singer, 2010). However, the mechanisms by which that happens and its impact on the circuit are
202 difficult to elucidate. Thus, we next investigated whether cortical organoids could be used to model
203 oscillatory network defects. Previous work evidenced that patients with autism spectrum disorder
204 exhibit reduced alpha oscillation power (8-12 Hz) and evoked gamma (40-60 Hz) response, as
205 well as reduced PAC (Khan *et al.*, 2013; Mohammad-Rezazadeh *et al.*, 2016). Mutations in the
206 Methyl-CpG-binding protein 2 (*MECP2*) gene lead to a severe disruption in cortical development
207 that account for many symptoms of Rett syndrome, autism, schizophrenia and other neurological
208 disorders (Amir *et al.*, 1999; Cohen *et al.*, 2002; Du *et al.*, 2016; Liu *et al.*, 2016; Wen *et al.*, 2017).
209 *MECP2* is involved in the epigenetic regulation of target genes by binding to methylated CpG

210 dinucleotides promoter regions, acting as a transcriptional modulator (Figure 4A).

211 To model MECP2 deficiency during neurodevelopment, we generated pluripotent stem
212 cell model with two different cell lines, each carrying a distinct *MECP2* mutation that lead to a
213 nonfunctional protein (Figure S9). Human *MECP2*-mutant neurons *in vitro* exhibit fewer synapses,
214 smaller soma size, altered calcium signaling and electrophysiological defects compared to
215 controls (Marchetto *et al.*, 2010). Based on the observed reduction in the number of layer V
216 neurons in *Mecp2*-mutant mice (Stuss *et al.*, 2012) and documented clinical data of microcephaly
217 in Rett syndrome patients (Amir *et al.*, 1999), we sought to examine transcriptomics, cellular and
218 structural differences using MECP2-KO cortical organoids. The delay in the maturation process
219 was accompanied by a significant decrease in the diameter of MECP2-KO organoids, spine-like
220 density and synaptic puncta at later stages of differentiation (Figure 4B-D). Additionally, a
221 significant reduction in the proportion of CTIP2+ and SATB2+ neurons was observed by targeted
222 single-cell analysis (Figure 4E-G) and corroborated by immunostaining (Figure 4h). MECP2-KO
223 cortical organoids also showed reduced neural activity leading to an absence of network
224 oscillations, which supports a delay in the maturation process (Figure 4I and 4J). The inability to
225 entrain into a functionally connected network at early stages of development might underlie the
226 core deficits found in MECP2-deficient related disorders. More importantly, these results highlight
227 the contribution of specific genes in the formation of a network circuitry and the emergence of
228 oscillatory activity.



229

230 **Figure 4. MECP2 contribution to the emergence of network oscillations.** (A) MECP2-

231 knockout neurons (MECP2-KO) show reduced spine-like density and soma size compared to

232 controls. (B) Organoid diameter quantification (CTR, $n = 210$ organoids; KO, $n = 333$ organoids).

233 (C) Spine-like density and (D) synaptic puncta are reduced in MECP2-KO neurons. Scale bar, 50

234 μm . (E-H) Targeted single-cell analysis of neural markers and cortical layer-related genes over

235 defined control Ct value. In 3-month-old cortical organoids, a significant decrease in the number

236 of CTIP2+ and SATB2+ neurons was observed. (I) MECP2-KO cortical organoids show

237 decreased mean firing rate after 5 months of maturation ($n = 6$ organoid cultures).

238 (J) Lack of oscillatory network events in 5-month-old MECP2-KO organoids. Each trace represents a single

239 event during the same recording session. For B, C, D, G, H, I and J, data are shown as mean \pm

240 s.e.m.; * $P < 0.05$, ** $P < 0.01$, *** $P < 0.001$, unpaired Student's t -test.

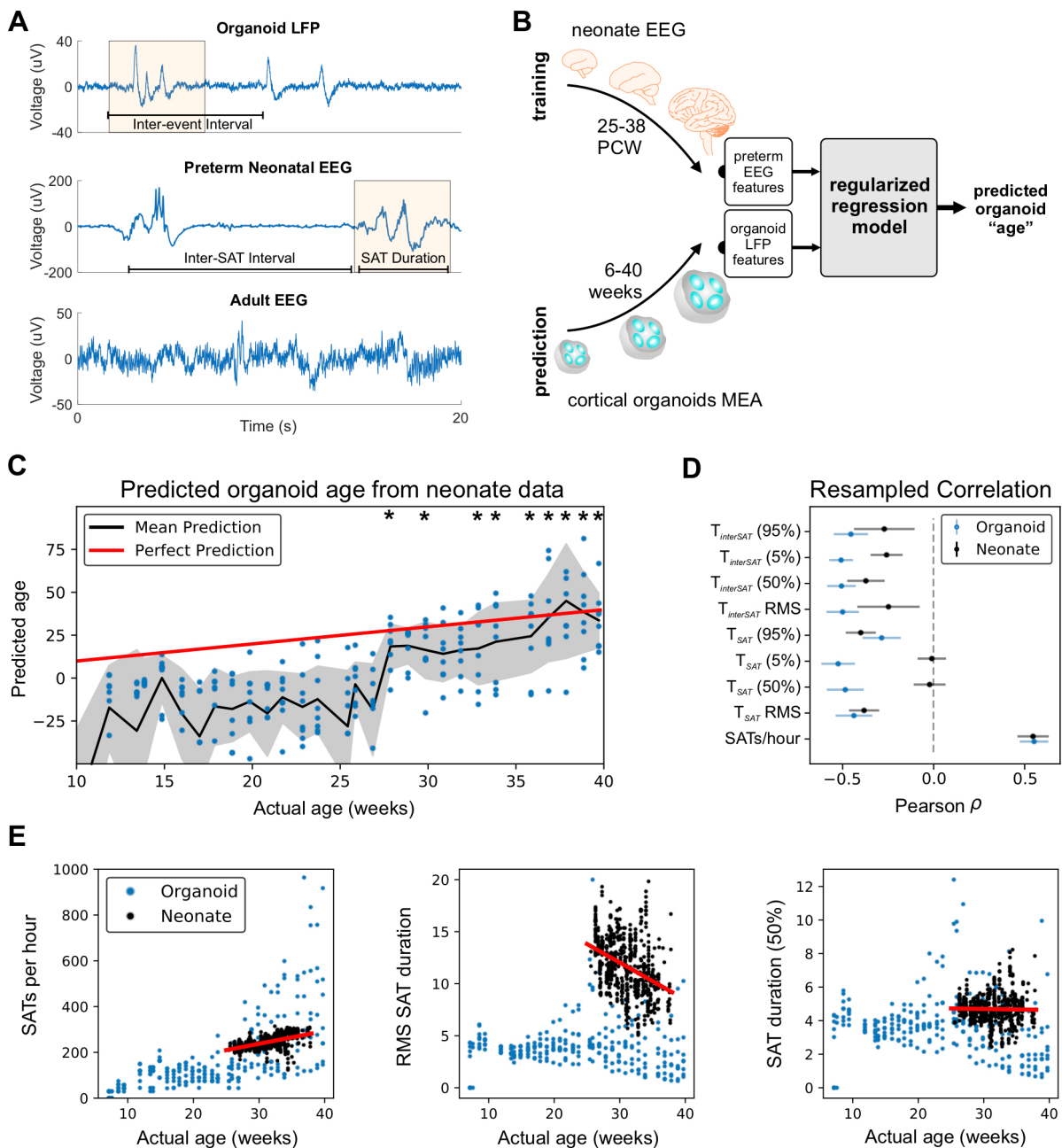
241

242 **Organoid network development recapitulates preterm EEG**

243 Despite similarities between the complex oscillatory network activity in organoids and the
244 *in vivo* brain, it is unclear whether the spontaneous developmental trajectory observed is
245 representative of programmed early neurodevelopment. While network activity from organoids
246 does not exhibit the full temporal complexity seen in adults, the pattern of alternating periods of
247 quiescence and network-synchronized events is similar to electrophysiological signatures present
248 in preterm human infant EEG. During *trace discontinu* (Tolonen *et al.*, 2007), quiescent periods
249 are punctuated by high-amplitude oscillations (spontaneous activity transients, SATs) lasting a
250 few seconds. Intervals of complete quiescence disappear as infants become of term, and the
251 EEG is dominated by continuous and low-amplitude desynchronized activity in adult brains
252 (Figure 5A). The time-frequency representation of network events in organoids also resembled
253 the oscillatory bursts in preterm EEG, with power localized in the low frequencies and often
254 accentuated within a narrow oscillatory band (Figure S10).

255 To quantitatively compare network activity in cortical organoids to preterm human EEG,
256 we trained (with cross-validation) a regularized regression model (L1 & L2 regularized, ElasticNet)
257 on a subset of features relating to SATs from a dataset of 567 preterm neonatal EEGs (Stevenson
258 *et al.*, 2017) (24-38 post-conception weeks, PCW). We emphasize that the regression model was
259 thus only optimized to predict preterm infant age based on their own brain features, and has not
260 seen any organoid data whatsoever up to this point. After training, we submitted analogous
261 features computed from organoid LFPs to the model and asked it to predict organoid “brain age”
262 over time (Figure 5B). Notably, the mean model-generated organoid “brain age” was
263 indistinguishable from its “true age” (*in vitro*) after 28 weeks (Figure 5C). In other words, organoids
264 past 28 weeks in culture exhibit similar developmental trajectories of electrophysiological features
265 as preterm neonates. Next, we examined the similarities between brain organoids and preterm
266 humans by looking at each specific feature (Figure 5C and 5D). Of all features, “SATs per hour”
267 (“events per hour” in organoids) showed strikingly similar values and growth, while “root-mean-

268 square SAT duration” showed a similar decline (but not in absolute value) over 25 to 38 weeks in
 269 both datasets (Figure 5E, S10B and 10C). Therefore, while the developmental trajectory of
 270 cortical organoids is not identical to that of the fetal brain, a machine learning model trained only
 271 on preterm neonatal EEG features was able to predict organoid culture age, demonstrating that
 272 the observed network electrophysiological features may share similarities representative of
 273 genetically programmed developmental timelines.



274

275 **Figure 5. Organoid network dynamics mimic premature neonates after 28 weeks of**
276 **maturation.** (A) Representative LFP trace from cortical organoid, highlighting instances of
277 network events (yellow). Comparable events between periods of quiescence (discontinuous
278 network dynamics) are shown in human preterm neonate EEG at 35 weeks gestational age, while
279 a different pattern of continuous activity is observed in adult EEG. SAT: spontaneous activity
280 transient. (B) Schematic of machine learning pipeline for organoid “brain-age” prediction: 9 EEG
281 features from 39 premature babies ($n = 567$ recordings) between 25 and 38 PCW were used to
282 train and cross-validate a regularized regression model (ElasticNet) to optimally predict neonate
283 brain age, which was then applied directly to organoid LFP features to predict organoid “brain-
284 age”. (C) Predicted organoid “brain age” plotted against actual organoid age. Black stars denote
285 time points where mean predicted age is not significantly different from actual age under 1-sample
286 t -test ($P < 0.05$, $n = 8$). (D) Resampled Pearson’s correlation coefficient between age and
287 electrophysiological features for both organoid and premature neonates show different degrees
288 of developmental similarity for individual features. (E) EEG/LFP features over time for organoids
289 and premature neonates show various levels of similarity.

290

291 **DISCUSSION**

292 Development of functional human brain networks is an activity-dependent process guided
293 by genetic and molecular programs, shaped by emerging cellular diversity. Neonatal neural
294 networks share many features with adult brains, despite the fundamental structural differences
295 (Power *et al.*, 2010). Even though the chronological stages of the human cortical network
296 formation are not well understood, it is suggested that emerging cognitive functions during infancy
297 are a result of different brain regions and environmental cues (Johnson, 2001). However, *in utero*
298 development is vital for the establishment of neuronal circuitry and healthy functioning of the brain.
299 The second and third trimester of gestation are when the corticothalamic network is formed *via*
300 transient connections of the subplate GABAergic neurons and the emergence of synchronized

301 network activity (Kostović and Judaš, 2010). Thus, early cortical functional maturation follows an
302 independent sensory-input pathway, guided by spontaneous activity and associated with synaptic
303 regulating mechanisms (Uhlhaas et al., 2010).

304 Here we report the formation of small-scale functional electrophysiological networks in
305 cortical organoids, similar to those observed in the developing brain. While we do not claim
306 functional equivalence between the organoids and a full neonatal cortex, the current results
307 represent the first step towards an *in vitro* model that captures the complex spatiotemporal
308 oscillatory dynamics of the human brain. Robust extracellular electrical activity was established
309 at earlier stages and progressively developed into an organized oscillatory network similar to that
310 observed in human EEG. As such, we show that features of early functional network dynamics
311 (e.g., spontaneous activity transients) can be recapitulated by an *in vitro* model of the developing
312 cortex, with no additional constraints other than structural and genetic similarities. This offers
313 strong evidence for a convergent experience-independent neurodevelopmental program of the
314 neocortex prior to birth. Given the potential roles of synchronized and oscillatory network
315 dynamics in coordinating information flow between developed cortical brain regions during human
316 cognition (Uhlhaas et al., 2010), these results highlight the potential for cortical organoids to
317 advance our understanding of functional electrophysiology, brain development, and neuro-
318 genetic disorders. Finally, our findings may ultimately reframe the ethical discussions on human
319 brain organoid research and offer an innovative link between microscale organoid physiology and
320 cognitive neuroscience.

321

322 **REFERENCES**

- 323
- 324 Allene, C., Cattani, A., Ackman, J.B., Bonifazi, P., Aniksztejn, L., Ben-Ari, Y., and Cossart, R.
325 (2008). Sequential Generation of Two Distinct Synapse-Driven Network Patterns in
326 Developing Neocortex. *J. Neurosci.* *28*, 12851–12863.
- 327 Amin, H., Maccione, A., Marinaro, F., Zordan, S., Nieuws, T., and Berdondini, L. (2016). Electrical
328 Responses and Spontaneous Activity of Human iPS-Derived Neuronal Networks
329 Characterized for 3-month Culture with 4096-Electrode Arrays. *Front. Neurosci.* *10*, 121.
- 330 Amir, R.E., Van den Veyver, I.B., Wan, M., Tran, C.Q., Francke, U., and Zoghbi, H.Y. (1999).
331 Rett syndrome is caused by mutations in X-linked MECP2, encoding methyl-CpG-binding
332 protein 2. *Nat. Genet.* *23*, 185–188.
- 333 Bardy, C., van den Hurk, M., Eames, T., Marchand, C., Hernandez, R. V., Kellogg, M., Gorris,
334 M., Galet, B., Palomares, V., Brown, J., et al. (2015). Neuronal medium that supports
335 basic synaptic functions and activity of human neurons in vitro. *Proc. Natl. Acad. Sci.* *112*,
336 E2725–E2734.
- 337 Barz, F., Livi, A., Lanzilotto, M., Maranesi, M., Bonini, L., Paul, O., and Ruther, P. (2017).
338 Versatile, modular 3D microelectrode arrays for neuronal ensemble recordings: from
339 design to fabrication, assembly, and functional validation in non-human primates. *J.*
340 *Neural Eng.* *14*, 036010.
- 341 Ben-Ari, Y. (2001). Developing networks play a similar melody. *Trends Neurosci.* *24*, 353–360.
- 342 Birey, F., Andersen, J., Makinson, C.D., Islam, S., Wei, W., Huber, N., Fan, H.C., Metzler,
343 K.R.C., Panagiotakos, G., Thom, N., et al. (2017). Assembly of functionally integrated
344 human forebrain spheroids. *Nature* *545*, 54–59.
- 345 Blankenship, A.G., and Feller, M.B. (2010). Mechanisms underlying spontaneous patterned
346 activity in developing neural circuits. *Nat. Rev. Neurosci.* *11*, 18–29.
- 347 Brown, J.P., Hall, D., Frank, C.L., Wallace, K., Mundy, W.R., and Shafer, T.J. (2016). Editor's
348 Highlight: Evaluation of a Microelectrode Array-Based Assay for Neural Network Ontogeny
349 Using Training Set Chemicals. *Toxicol. Sci.* *154*, 126–139.
- 350 Buzsáki, G., and Draguhn, A. (2004). Neuronal oscillations in cortical networks. *Science* *304*,
351 1926–1929.
- 352 Buzsáki, G., Anastassiou, C.A., and Koch, C. (2012). The origin of extracellular fields and
353 currents — EEG, ECoG, LFP and spikes. *Nat. Rev. Neurosci.* *13*, 407–420.
- 354 Buzsáki, G., Logothetis, N., and Singer, W. (2013). Scaling Brain Size, Keeping Timing:
355 Evolutionary Preservation of Brain Rhythms. *Neuron* *80*, 751–764.
- 356 Camp, J.G., Badsha, F., Florio, M., Kanton, S., Gerber, T., Wilsch-Bräuninger, M., Lewitus, E.,
357 Sykes, A., Hevers, W., Lancaster, M., et al. (2015). Human cerebral organoids
358 recapitulate gene expression programs of fetal neocortex development. *Proc. Natl. Acad.*
359 *Sci.* *112*, 201520760.
- 360 Cesca, F., Satapathy, A., Ferrea, E., Nieuws, T., Benfenati, F., and Scholz-Starke, J. (2015).
361 Functional Interaction between the Scaffold Protein Kidins220/ARMS and Neuronal
362 Voltage-Gated Na⁺ Channels. *J. Biol. Chem.* *290*, 18045–18055.
- 363 Chen, L., Deng, Y., Luo, W., Wang, Z., and Zeng, S. (2009). Detection of bursts in neuronal
364 spike trains by the mean inter-spike interval method. *Prog. Nat. Sci.* *19*, 229–235.
- 365 Clements, I.P., Millard, D.C., Nicolini, A.M., Preyer, A.J., Grier, R., Heckerling, A., Blum, R.A.,
366 Tyler, P., McSweeney, K.M., Lu, Y.-F., et al. (2016). Optogenetic stimulation of multiwell
367 MEA plates for neural and cardiac applications. In *Proceedings of the SPIE, Volume 9690*,
368 *Id. 96902C 10 Pp.* (2016)., S.J. Madsen, V.X.D. Yang, E.D. Jansen, Q. Luo, S.K.
369 Mohanty, and N. V. Thakor, eds. p. 96902C.
- 370 Cohen, D., Lazar, G., Couvert, P., Desportes, V., Lippe, D., Mazet, P., and Héron, D. (2002).
371 MECP2 mutation in a boy with language disorder and schizophrenia. *Am. J. Psychiatry*
372 *159*, 148–149.

- 373 Cotterill, E., Hall, D., Wallace, K., Mundy, W.R., Eglon, S.J., and Shafer, T.J. (2016).
374 Characterization of Early Cortical Neural Network Development in Multiwell Microelectrode
375 Array Plates. *J. Biomol. Screen.* *21*, 510–519.
- 376 Du, F., Nguyen, M.V.C., Karten, A., Felice, C.A., Mandel, G., and Ballas, N. (2016). Acute and
377 crucial requirement for MeCP2 function upon transition from early to late adult stages of
378 brain maturation. *Hum. Mol. Genet.* *25*, 1690–1702.
- 379 Fries, P. (2005). A mechanism for cognitive dynamics: neuronal communication through
380 neuronal coherence. *Trends Cogn. Sci.* *9*, 474–480.
- 381 Gao, R., Peterson, E.J., and Voytek, B. (2017). Inferring synaptic excitation/inhibition balance
382 from field potentials. *Neuroimage* *158*, 70–78.
- 383 Gore, A., Li, Z., Fung, H.-L., Young, J.E., Agarwal, S., Antosiewicz-Bourget, J., Canto, I.,
384 Giorgetti, A., Israel, M.A., Kiskinis, E., et al. (2011). Somatic coding mutations in human
385 induced pluripotent stem cells. *Nature* *471*, 63–67.
- 386 Harrill, J.A., Chen, H., Streifel, K.M., Yang, D., Mundy, W.R., and Lein, P.J. (2015). Ontogeny of
387 biochemical, morphological and functional parameters of synaptogenesis in primary
388 cultures of rat hippocampal and cortical neurons. *Mol. Brain* *8*, 10.
- 389 de Hemptinne, C., Swann, N.C., Ostrem, J.L., Ryapolova-Webb, E.S., San Luciano, M.,
390 Galifianakis, N.B., and Starr, P.A. (2015). Therapeutic deep brain stimulation reduces
391 cortical phase-amplitude coupling in Parkinson’s disease. *Nat. Neurosci.* *18*, 779–786.
- 392 Henriques, J.B., and Davidson, R.J. (1991). Left frontal hypoactivation in depression. *J.*
393 *Abnorm. Psychol.* *100*, 535–545.
- 394 Johnson, M.H. (2001). Functional brain development in humans. *Nat. Rev. Neurosci.* *2*, 475–
395 483.
- 396 Kelava, I., and Lancaster, M.A.A. (2016). Stem Cell Models of Human Brain Development. *Cell*
397 *Stem Cell* *18*, 736–748.
- 398 Khan, S., Gramfort, A., Shetty, N.R., Kitzbichler, M.G., Ganesan, S., Moran, J.M., Lee, S.M.,
399 Gabrieli, J.D.E., Tager-Flusberg, H.B., Joseph, R.M., et al. (2013). Local and long-range
400 functional connectivity is reduced in concert in autism spectrum disorders. *Proc. Natl.*
401 *Acad. Sci. U. S. A.* *110*, 3107–3112.
- 402 Khazipov, R., and Luhmann, H.J. (2006). Early patterns of electrical activity in the developing
403 cerebral cortex of humans and rodents. *Trends Neurosci.* *29*, 414–418.
- 404 Kostović, I., and Judaš, M. (2010). The development of the subplate and thalamocortical
405 connections in the human foetal brain. *Acta Paediatr.* *99*, 1119–1127.
- 406 Lancaster, M.A., and Knoblich, J.A. (2014). Generation of cerebral organoids from human
407 pluripotent stem cells. *Nat. Protoc.* *9*, 2329–2340.
- 408 Lancaster, M. a, Renner, M., Martin, C.-A., Wenzel, D., Bicknell, L.S., Hurles, M.E., Homfray, T.,
409 Penninger, J.M., Jackson, A.P., and Knoblich, J. a (2013). Cerebral organoids model
410 human brain development and microcephaly. *Nature* *501*, 373–379.
- 411 van de Leemput, J., Boles, N.C., Kiehl, T.R., Corneo, B., Lederman, P., Menon, V., Lee, C.,
412 Martinez, R.A., Levi, B.P., Thompson, C.L., et al. (2014). CORTECON: a temporal
413 transcriptome analysis of in vitro human cerebral cortex development from human
414 embryonic stem cells. *Neuron* *83*, 51–68.
- 415 Lisman, J. (1997). Bursts as a unit of neural information: making unreliable synapses reliable.
416 *Trends Neurosci.* *20*, 38–43.
- 417 Liu, Z., Li, X., Zhang, J.-T., Cai, Y.-J., Cheng, T.-L., Cheng, C., Wang, Y., Zhang, C.-C., Nie, Y.-
418 H., Chen, Z.-F., et al. (2016). Autism-like behaviours and germline transmission in
419 transgenic monkeys overexpressing MeCP2. *Nature* *530*, 98–102.
- 420 Luo, C., Lancaster, M.A., Castanon, R., Nery, J.R., Knoblich, J.A., and Ecker, J.R. (2016).
421 Cerebral Organoids Recapitulate Epigenomic Signatures of the Human Fetal Brain. *Cell*
422 *Rep.* *17*, 3369–3384.
- 423 Manning, J.R., Jacobs, J., Fried, I., and Kahana, M.J. (2009). Broadband Shifts in Local Field

- 424 Potential Power Spectra Are Correlated with Single-Neuron Spiking in Humans. *J.*
425 *Neurosci.* **29**, 13613–13620.
- 426 Marchetto, M.C., Belinson, H., Tian, Y., Freitas, B.C., Fu, C., Vadodaria, K.C., Beltrao-Braga,
427 P.C., Trujillo, C.A., Mendes, A.P.D., Padmanabhan, K., et al. (2017). Altered proliferation
428 and networks in neural cells derived from idiopathic autistic individuals. *Mol. Psychiatry*
429 **22**, 820–835.
- 430 Marchetto, M.C.N.N., Carromeu, C., Acab, A., Yu, D., Yeo, G.W., Mu, Y., Chen, G., Gage, F.H.,
431 and Muotri, A.R. (2010). A model for neural development and treatment of Rett syndrome
432 using human induced pluripotent stem cells. *Cell* **143**, 527–539.
- 433 Mariani, J., Simonini, M. V., Palejev, D., Tomasini, L., Coppola, G., Szekely, A.M., Horvath, T.L.,
434 and Vaccarino, F.M. (2012). Modeling human cortical development in vitro using induced
435 pluripotent stem cells. *Proc. Natl. Acad. Sci.* **109**, 12770–12775.
- 436 McSweeney, K.M., Gussow, A.B., Bradrick, S.S., Dugger, S.A., Gelfman, S., Wang, Q.,
437 Petrovski, S., Frankel, W.N., Boland, M.J., and Goldstein, D.B. (2016). Inhibition of
438 microRNA 128 promotes excitability of cultured cortical neuronal networks. *Genome Res.*
439 **26**, 1411–1416.
- 440 Miller, K.J., Leuthardt, E.C., Schalk, G., Rao, R.P.N., Anderson, N.R., Moran, D.W., Miller, J.W.,
441 and Ojemann, J.G. (2007). Spectral Changes in Cortical Surface Potentials during Motor
442 Movement. *J. Neurosci.* **27**, 2424–2432.
- 443 Mohammad-Rezazadeh, I., Frohlich, J., Loo, S.K., and Jeste, S.S. (2016). Brain connectivity in
444 autism spectrum disorder. *Curr. Opin. Neurol.* **29**, 137–147.
- 445 Mukamel, R., Gelbard, H., Arieli, A., Hasson, U., Fried, I., and Malach, R. (2005). Coupling
446 Between Neuronal Firing, Field Potentials, and fMRI in Human Auditory Cortex. *Science*
447 **309**, 951–954.
- 448 Nageshappa, S., Carromeu, C., Trujillo, C.A., Mesci, P., Espuny-Camacho, I., Pasciuto, E.,
449 Vanderhaeghen, P., Verfaillie, C.M., Raitano, S., Kumar, A., et al. (2016). Altered neuronal
450 network and rescue in a human MECP2 duplication model. *Mol. Psychiatry* **21**, 178–188.
- 451 Odawara, A., Saitoh, Y., Alhebshi, A.H., Gotoh, M., and Suzuki, I. (2014). Long-term
452 electrophysiological activity and pharmacological response of a human induced
453 pluripotent stem cell-derived neuron and astrocyte co-culture. *Biochem. Biophys. Res.*
454 *Commun.* **443**, 1176–1181.
- 455 Odawara, A., Katoh, H., Matsuda, N., and Suzuki, I. (2016). Physiological maturation and drug
456 responses of human induced pluripotent stem cell-derived cortical neuronal networks in
457 long-term culture. *Sci. Rep.* **6**, 26181.
- 458 Opitz, T., De Lima, A.D., and Voigt, T. (2002). Spontaneous Development of Synchronous
459 Oscillatory Activity During Maturation of Cortical Networks In Vitro. *J. Neurophysiol.* **88**,
460 2196–2206.
- 461 Paşca, A.M., Sloan, S.A., Clarke, L.E., Tian, Y., Makinson, C.D., Huber, N., Kim, C.H., Park, J.-
462 Y., O'Rourke, N.A., Nguyen, K.D., et al. (2015). Functional cortical neurons and astrocytes
463 from human pluripotent stem cells in 3D culture. *Nat. Methods* **12**, 671–678.
- 464 Paşca, S.P. (2018). The rise of three-dimensional human brain cultures. *Nature* **553**, 437–445.
- 465 Pedregosa, F., Varoquaux, G., Gramfort, A., Michel, V., Thirion, B., Grisel, O., Blondel, M.,
466 Prettenhofer, P., Weiss, R., Dubourg, V., et al. (2011). Scikit-learn: Machine Learning in
467 Python. *J. Mach. Learn. Res.* **12**, 2825–2830.
- 468 Power, J.D., Fair, D.A., Schlaggar, B.L., and Petersen, S.E. (2010). The Development of Human
469 Functional Brain Networks. *Neuron* **67**, 735–748.
- 470 Qian, X., Nguyen, H.N., Song, M.M., Hadiono, C., Ogden, S.C., Hammack, C., Yao, B.,
471 Hamersky, G.R., Jacob, F., Zhong, C., et al. (2016). Brain-Region-Specific Organoids
472 Using Mini-bioreactors for Modeling ZIKV Exposure. *Cell* **165**, 1238–1254.
- 473 Quadrato, G., Nguyen, T., Macosko, E.Z., Sherwood, J.L., Min Yang, S., Berger, D.R., Maria,
474 N., Scholvin, J., Goldman, M., Kinney, J.P., et al. (2017). Cell diversity and network

- 475 dynamics in photosensitive human brain organoids. *Nature* 545, 48–53.
- 476 Quiroga, R.Q., Nadasdy, Z., and Ben-Shaul, Y. (2004). Unsupervised spike detection and
477 sorting with wavelets and superparamagnetic clustering. *Neural Comput.* 16, 1661–1687.
- 478 Renner, M., Lancaster, M.A., Bian, S., Choi, H., Ku, T., Peer, A., Chung, K., and Knoblich, J.A.
479 (2017). Self-organized developmental patterning and differentiation in cerebral organoids.
480 *EMBO J.* 36, 1316–1329.
- 481 Roy, S., Zhao, L., and Wang, X. (2016). Distinct Neural Activities in Premotor Cortex during
482 Natural Vocal Behaviors in a New World Primate, the Common Marmoset (*Callithrix*
483 *jacchus*). *J. Neurosci.* 36, 12168–12179.
- 484 Stevenson, N.J., Oberdorfer, L., Koolen, N., O’Toole, J.M., Werther, T., Klebermass-Schrehof,
485 K., and Vanhatalo, S. (2017). Functional maturation in preterm infants measured by serial
486 recording of cortical activity. *Sci. Rep.* 7, 12969.
- 487 Strickland, J.D., LeFew, W.R., Crooks, J., Hall, D., Ortenzio, J.N.R., Dreher, K., and Shafer, T.J.
488 (2016). In vitro screening of silver nanoparticles and ionic silver using neural networks
489 yields differential effects on spontaneous activity and pharmacological responses.
490 *Toxicology* 355–356, 1–8.
- 491 Stuss, D.P., Boyd, J.D., Levin, D.B., and Delaney, K.R. (2012). MeCP2 Mutation Results in
492 Compartment-Specific Reductions in Dendritic Branching and Spine Density in Layer 5
493 Motor Cortical Neurons of YFP-H Mice. *PLoS One* 7, e31896.
- 494 Tetzlaff, C., Okujeni, S., Egert, U., Wörgötter, F., and Butz, M. (2010). Self-organized criticality
495 in developing neuronal networks. *PLoS Comput. Biol.* 6, e1001013.
- 496 Chailangkarn, T., Trujillo, C.A., Freitas, B.C., Hrvoj-Mihic, B., Herai, R.H., Yu, D.X., Brown, T.T.,
497 Marchetto, M.C., Bardy, C., McHenry, L., et al. (2016). A human neurodevelopmental
498 model for Williams syndrome. *Nature* 536, 338–343.
- 499 Thomas, C.A., Tejwani, L., Trujillo, C.A., Negraes, P.D., Herai, R.H., Mesci, P., Macia, A., Crow,
500 Y.J., and Muotri, A.R. (2017). Modeling of TREX1-Dependent Autoimmune Disease using
501 Human Stem Cells Highlights L1 Accumulation as a Source of Neuroinflammation. *Cell*
502 *Stem Cell* 21, 319–331.e8.
- 503 Tolonen, M., Palva, J.M., Andersson, S., and Vanhatalo, S. (2007). Development of the
504 spontaneous activity transients and ongoing cortical activity in human preterm babies.
505 *Neuroscience* 145, 997–1006.
- 506 Tort, A.B.L., Komorowski, R., Eichenbaum, H., and Kopell, N. (2010). Measuring Phase-
507 Amplitude Coupling Between Neuronal Oscillations of Different Frequencies. *J.*
508 *Neurophysiol.* 104, 1195–1210.
- 509 Tukker, A.M., de Groot, M.W.G.D.M., Wijnolts, F.M.J., Kasteel, E.E.J., Hondebrink, L., and
510 Westerink, R.H.S. (2016). Is the time right for in vitro neurotoxicity testing using human
511 iPSC-derived neurons? *ALTEX* 33, 261–271.
- 512 Uesaka, N., Hayano, Y., Yamada, A., and Yamamoto, N. (2007). Interplay between laminar
513 specificity and activity-dependent mechanisms of thalamocortical axon branching. *J.*
514 *Neurosci.* 27, 5215–5223.
- 515 Uhlhaas, P.J., and Singer, W. (2010). Abnormal neural oscillations and synchrony in
516 schizophrenia. *Nat. Rev. Neurosci.* 11, 100–113.
- 517 Uhlhaas, P.J., Roux, F., Rodriguez, E., Rotarska-Jagiela, A., and Singer, W. (2010). Neural
518 synchrony and the development of cortical networks. *Trends Cogn. Sci.* 14, 72–80.
- 519 Vessoni, A.T., Herai, R.H., Karpiak, J. V., Leal, A.M.S., Trujillo, C.A., Quinet, A., Agnez Lima,
520 L.F., Menck, C.F.M., and Muotri, A.R. (2016). Cockayne syndrome-derived neurons
521 display reduced synapse density and altered neural network synchrony. *Hum. Mol. Genet.*
522 25, 1271–1280.
- 523 Voytek, B., and Knight, R.T. (2015). Dynamic network communication as a unifying neural basis
524 for cognition, development, aging, and disease. *Biol. Psychiatry* 77, 1089–1097.
- 525 Voytek, B., Kayser, A.S., Badre, D., Fegen, D., Chang, E.F., Crone, N.E., Parvizi, J., Knight,

- 526 R.T., and D'Esposito, M. (2015). Oscillatory dynamics coordinating human frontal
527 networks in support of goal maintenance. *Nat. Neurosci.* *18*, 1318–1324.
- 528 Wallace, K., Strickland, J.D., Valdivia, P., Mundy, W.R., and Shafer, T.J. (2015). A multiplexed
529 assay for determination of neurotoxicant effects on spontaneous network activity and
530 viability from microelectrode arrays. *Neurotoxicology* *49*, 79–85.
- 531 Wen, Z., Cheng, T.-L., Li, G.-Z., Sun, S.-B., Yu, S.-Y., Zhang, Y., Du, Y.-S., and Qiu, Z. (2017).
532 Identification of autism-relatedMECP2mutations by whole-exome sequencing and
533 functional validation. *Mol. Autism* *8*, 43.
- 534 Xu, X., Tay, Y., Sim, B., Yoon, S.-I., Huang, Y., Ooi, J., Utami, K.H., Ziaei, A., Ng, B.,
535 Radulescu, C., et al. (2017). Reversal of Phenotypic Abnormalities by CRISPR/Cas9-
536 Mediated Gene Correction in Huntington Disease Patient-Derived Induced Pluripotent
537 Stem Cells. *Stem Cell Reports* *8*, 619–633.
- 538 Yang, Y., Huang, J., Mis, M.A., Estacion, M., Macala, L., Shah, P., Schulman, B.R., Horton,
539 D.B., Dib-Hajj, S.D., and Waxman, S.G. (2016). Nav1.7-A1632G Mutation from a Family
540 with Inherited Erythromelalgia: Enhanced Firing of Dorsal Root Ganglia Neurons Evoked
541 by Thermal Stimuli. *J. Neurosci.* *36*, 7511–7522.
- 542 Zhang, Z.-N.Z.-N., Freitas, B.C.B.C., Qian, H., Lux, J., Acab, A., Trujillo, C.A.C.A., Herai,
543 R.H.R.H., Huu, V.A.N., Wen, J.H.J.H., Joshi-Barr, S., et al. (2016). Layered hydrogels
544 accelerate iPSC-derived neuronal maturation and reveal migration defects caused by
545 MeCP2 dysfunction. *113*, 3185–3190.
- 546
- 547
- 548
- 549

550 **SUPPLEMENTARY INFORMATION**

551 Supplemental information includes Supplemental Experimental Procedures, 10 Figures, 2 tables
552 can be found with this article online.

553

554 **ACKNOWLEDGMENTS**

555 This work was supported by grants from the California Institute for Regenerative Medicine (CIRM)
556 DISC1-08825 and DISC2-09649, the National Institutes of Health through the R01MH108528,
557 R01MH094753, R01MH109885, R01MH100175, R56MH109587, a SFARI grant #345469, and a
558 NARSAD Independent Investigator Grant to A.R.M. B.V is supported by a Sloan Research
559 Fellowship, the Whitehall Foundation (2017-12-73), and the National Science Foundation
560 (1736028). I.A.C. is a San Diego IRACDA Fellow supported by National Institutes of Health
561 (NIH)/NIGMS K12 GM06852 Award. G.W.Y. and A.R.M. are supported by U19MH1073671, part
562 of the National Cooperative Reprogrammed Cell Research Groups (NCRCRG) to Study Mental
563 Illness. R.G is supported by the Natural Sciences and Engineering Research Council of Canada
564 (NSERC PGS-D), UCSD Kavli Innovative Research Grant (IRG), Frontiers for Innovation
565 Scholars Program, and Katzin Prize. We thank Patrick S. Cooper for his help on the Australian
566 EEG Database.

567

568 **AUTHOR CONTRIBUTIONS**

569 C.A.T., R.G. and P.D.N. should be considered co-first authors as they each designed the
570 experiments and conducted the analyses with input from A.R.M., B.V.; P.D.N. and C.A.T.
571 generated and characterized the cortical organoids and performed the MEA recordings. C.A.T.
572 performed C1 single-cell analyses and synaptic quantification. I.A.C. performed and analyzed
573 10X Genomics single-cell experiments. A.Do. processed 10X Genomics single-cell data. G.W.Y.
574 led and funded the single-cell RNA-seq analyses. M.V. and A.De. performed the functional
575 experiment. P.D.N. analyzed the MEA data using the Axion Biosystems Neural Metrics Tool. R.G.

576 performed the custom MEA and EEG analyses. A.R.M. and B.V. should be considered co-senior
577 authors as they contributed equally to directing the overall study design, with A.R.M. leading the
578 cortical organoid development and analyses, and B.V. leading the electrophysiological design
579 and analyses. C.A.T., R.G., P.D.N., B.V. and A.R.M wrote the manuscript. All authors reviewed
580 the manuscript for publication.

581

582 **CONFLICT OF INTERESTS**

583 Dr. Muotri is a co-founder and has equity interest in TISMOO, a company dedicated to genetic
584 analysis focusing on therapeutic applications customized for autism spectrum disorder and other
585 neurological disorders with genetic origins. The terms of this arrangement have been reviewed
586 and approved by the University of California San Diego in accordance with its conflict of interest
587 policies.

588

589 **AUTHOR INFORMATION**

590 Correspondence and requests for materials should be addressed to muotri@ucsd.edu or
591 bvoytek@ucsd.edu.

592

593

594

595

596

597

598

599 **FIGURE LEGENDS**

600 **Figure 1. Cellular and molecular development of human cortical organoids.** (A) Overview of
601 human neural network formation and dynamics evaluation using organoids. (B) Schematic of the
602 protocol used to generate cortical organoids. Scale bar, 200 μm . (C) Organoid growth during
603 different developmental stages. (D) Representative immunostainings showing proliferating NPCs
604 (Ki67+ and Nestin+), lower (TBR1+ and CTIP2+) and upper (SATB2+) cortical layer neurons and
605 glial cells (GFAP+) overtime. Scale bar, 50 μm . (E) Population analysis of specific markers
606 indicating stages of maturation and multiple neuronal subtypes. The data are shown as mean \pm
607 s.e.m. ($n = 8$). (F) Representative image of a pyramidal neuron (left panel); dendritic spine-like
608 structures (arrow) are observed in cells transduced with the SYN:EGFP reporter (middle panel;
609 scale bar, 5 μm). Immunohistochemical detection of the synaptic protein Syn1 (right panel; scale
610 bar, 50 μm). (G) Electron microscopy of synaptic structures in 4-month-old cortical organoids
611 (blue). (H) *t*-distributed stochastic neighbor embedding (*t*SNE) plot of 3,491 cells from 6-month-
612 old organoids. Colors denote seven main cell clusters. (I) *t*SNE plots depicting cell-type specific
613 marker expression levels (red denotes higher expression). (J) Heatmap of average expression
614 for representative gene markers by cluster and cell-type (see also Figure S4). (K) Violin plots
615 showing transcript levels for representative markers of each cluster (see Figure S3 for additional
616 markers).

617
618 **Figure 2. Oscillatory network dynamics in long-term cortical organoids.** (A) Schematic of
619 the organoid signal processing pipeline. Raw MEA data is analyzed as population spiking and
620 LFP separately. Synchronous network events are highlighted in yellow. (B) Raster plot of network
621 spiking activity after 1.5 and 6 months of maturation. A 3-s interval of activity over 5 channels is
622 shown in the upper right corners. (C) Cortical organoids show elevated and continuously
623 increasing mean firing rate compared to 2D monolayer neurons ($n = 8$ organoid cultures, and $n =$
624 12 for 2D neurons). Inset, correlation of the firing rate vector over 12 weeks of differentiation (from

625 8 to 20) between pairs of cultures showing reduced variability among organoid replicates. (D)
626 Temporal evolution of cortical organoid network activity. Detailed definitions and further
627 parameters are presented in Figure 5B and 5C. (E) Time series of population spiking and LFP
628 during network events in cortical organoid development. Each trace represents a single event
629 during the same recording session. (F) Oscillatory dynamics within network events develop
630 nonlinearly, following an inverted-U trajectory. (G) Increase of network variability dynamics
631 throughout development. (H) Oscillatory power increases up to the 25th week in culture and
632 plateaus at 30 weeks. Inset, Oscillatory power is calculated by fitting a straight line (dashed) over
633 the aperiodic portion of the PSD and taken as the height of narrow peaks rising above the linear
634 fit. The data shown in C, D, F, G and H are presented as mean \pm s.e.m. *P < 0.05, **P < 0.01,
635 ***P < 0.001, unpaired Student's *t*-test (C), quadratic (F) and linear (G) regression.

636

637 **Figure 3. Cortical organoid serves as a model of functional oscillations and their synaptic**
638 **mechanisms.** (A-C) Phase-amplitude coupling is observed in organoid LFP during network
639 events, a phenomenon proposed to mediate neural communication *in vivo*. (A) Example of raw
640 LFP during a network event decomposed into its low-frequency component (1-4 Hz delta) and the
641 amplitude envelope of the high-frequency, broadband gamma component (200-400 Hz). Analysis
642 was repeated for 100-200 Hz with near identical effect size and significance. (B) Normalized
643 gamma amplitude binned by delta phase during network events (black) shows greater modulation
644 depth by low frequency delta than during non-event periods (red). (C) Phase-amplitude coupling
645 during network events is significantly greater than non-event periods in all batches. (D) Effect of
646 selective drug treatments on neuronal electrical activity in 6-month-old organoids. Representative
647 raster plots and burst measurements of untreated and treated organoids. Scale bar, 20 s.
648 Exposure to AP5 + CNQX, baclofen and muscimol reversibly extinguish the network bursts
649 (synchrony), while no changes were promoted by bicuculline. (E-F) Pharmacological perturbation
650 of oscillatory activity during network events in 6-month-old organoids. Application of bicuculline

651 increases the number of network events, while CNQX + AP5 and baclofen completely abolish
652 synchronized network events. Bicuculline blocks oscillatory network activity but not the network
653 event itself. Data are shown as mean \pm s.e.m.; unpaired Student's *t*-test.

654

655 **Figure 4. MECP2 contribution to the emergence of network oscillations.** (A) MECP2-
656 knockout neurons (MECP2-KO) show reduced spine-like density and soma size compared to
657 controls. (B) Organoid diameter quantification (CTR, $n = 210$ organoids; KO, $n = 333$ organoids).
658 (C) Spine-like density and (D) synaptic puncta are reduced in MECP2-KO neurons. Scale bar, 50
659 μ m. (E-H) Targeted single-cell analysis of neural markers and cortical layer-related genes over
660 defined control *Ct* value. In 3-month-old cortical organoids, a significant decrease in the number
661 of CTIP2+ and SATB2+ neurons was observed. (I) MECP2-KO cortical organoids show
662 decreased mean firing rate after 5 months of maturation ($n = 6$ organoid cultures). (J) Lack of
663 oscillatory network events in 5-month-old MECP2-KO organoids. Each trace represents a single
664 event during the same recording session. For B, C, D, G, H, I and J, data are shown as mean \pm
665 s.e.m.; * $P < 0.05$, ** $P < 0.01$, *** $P < 0.001$, unpaired Student's *t*-test.

666

667 **Figure 5. Organoid network dynamics mimic premature neonates after 28 weeks of**
668 **maturation.** (A) Representative LFP trace from cortical organoid, highlighting instances of
669 network events (yellow). Comparable events between periods of quiescence (discontinuous
670 network dynamics) are shown in human preterm neonate EEG at 35 weeks gestational age, while
671 a different pattern of continuous activity is observed in adult EEG. SAT: spontaneous activity
672 transient. (B) Schematic of machine learning pipeline for organoid "brain-age" prediction: 9 EEG
673 features from 39 premature babies ($n = 567$ recordings) between 25 and 38 PCW were used to
674 train and cross-validate a regularized regression model (ElasticNet) to optimally predict neonate
675 brain age, which was then applied directly to organoid LFP features to predict organoid "brain-
676 age". (C) Predicted organoid "brain age" plotted against actual organoid age. Black stars denote

677 time points where mean predicted age is not significantly different from actual age under 1-sample
678 *t*-test ($P < 0.05$, $n = 8$). (D) Resampled Pearson's correlation coefficient between age and
679 electrophysiological features for both organoid and premature neonates show different degrees
680 of developmental similarity for individual features. (E) EEG/LFP features over time for organoids
681 and premature neonates show various levels of similarity.

682

683

684 **EXPERIMENTAL PROCEDURES**

685 **Cell source.** iPSC lines derived from control individuals have been previously characterized
686 elsewhere (Gore et al., 2011; Nageshappa et al., 2016). Human embryonic stem cell (ESC) and
687 iPSC colonies were expanded on Matrigel-coated dishes (BD Biosciences, San Jose, CA, USA)
688 with mTeSR1 medium (StemCell Technologies, Vancouver, Canada). The cells were routinely
689 checked by karyotype and CNV arrays to avoid genomic alterations in the culture. The study was
690 approved by the University of California San Diego IRB/ESCRO committee (protocol 141223ZF).

691
692 **Teratoma formation.** iPSC colonies were dissociated, re-suspended in PBS-Matrigel, and
693 injected subcutaneously in NOD SCID mice. The tumor was dissected, fixed in and paraffin
694 embedded after 8 weeks. Sections of 10 μ m thickness were stained with hematoxylin and eosin,
695 and analyzed for the presence of the three germ layer tissues. Protocols were approved by the
696 UCSD Institutional Animal Care and Use Committee.

697
698 **MECP2-KO cell line generation.** MECP2-deficient cell lines were generated by inducing
699 pluripotency in fibroblasts derived from a male patient. Additionally, we used H9 human ESC with
700 the CRISPR/Cas9 genome-editing system to induce frameshift mutations in the *MECP2* locus.
701 This incorporation resulted in the creation of early stop codons rendering a non-functional MECP2
702 protein. Mutagenesis and off-targets were confirmed by exome sequencing techniques. The
703 CRISPR-Cas protocol can be found elsewhere (Thomas et al., 2017). Once we confirmed the
704 pluripotency state of the cellular models, we differentiated them into 2D neuronal monolayer
705 cultures (Thanathom et al., 2016) and cortical organoids.

706
707 **Generation of cortical organoids.** Feeder-free iPSCs were fed daily with mTeSR1 for 7 days.
708 Colonies were dissociated using Accutase (Life Technologies, Carlsbad, CA, USA) in PBS (1:1)
709 for 10 minutes at 37 °C and centrifuged for 3 minutes at 150 x g. The cell pellet was resuspended

710 in mTeSR1 supplemented with 10 μ M SB431542 (SB; Stemgent, Cambridge, MA, USA) and 1 μ M
711 Dorsomorphin (Dorso; R&D Systems, Minneapolis, MN, USA). Approximately 4×10^6 cells were
712 transferred to one well of a 6-well plate and kept in suspension under rotation (95 rpm) in the
713 presence of 5 μ M ROCK inhibitor (Y-27632; Calbiochem, Sigma-Aldrich, St. Louis, MO, USA) for
714 24 hours to form free-floating spheres. After 3 days, mTeSR1 was substituted by Media1
715 [Neurobasal (Life Technologies) supplemented with Glutamax, 2% Gem21 NeuroPlex (Gemini
716 Bio-Products, West Sacramento, CA, USA), 1% N2 NeuroPlex (Gemini Bio-Products), 1% MEM
717 nonessential amino acids (NEAA; Life Technologies), 1% penicillin/streptomycin (PS; Life
718 Technologies), 10 μ M SB and 1 μ M Dorso] for 7 days. Then, the cells were maintained in Media2
719 [Neurobasal with Glutamax, 2% Gem21 NeuroPlex, 1% NEAA and 1% PS] supplemented with
720 20 ng/mL FGF2 (Life Technologies) for 7 days, followed by 7 additional days in Media2
721 supplemented with 20 ng/mL of FGF2 and 20 ng/mL EGF (PeproTech, Rocky Hill, NJ, USA).
722 Next, cells were transferred to Media3 [Media2 supplemented with 10 μ g/mL of BDNF, 10 μ g/mL
723 of GDNF, 10 μ g/mL of NT-3 (all from PeproTech), 200 μ M L-ascorbic acid and 1 mM dibutyl-
724 cAMP (Sigma-Aldrich)]. After 7 days, cortical organoids were maintained in Media2 for as long as
725 needed, with media changes every 3-4 days.

726

727 **Mycoplasma testing.** All cellular cultures were routinely tested for mycoplasma by PCR. Media
728 supernatants (with no antibiotics) were collected, centrifuged, and resuspended in saline buffer.
729 Ten microliters of each sample were used for a PCR with the following primers: Forward:
730 GGCGAATGGGTGAGTAAC; Reverse: CGGATAACGCTTGCGACCT. Only negative samples
731 were used in the study.

732

733 **Immunofluorescence staining.** Cortical organoids were fixed with 4% paraformaldehyde
734 overnight at 4°C and then transferred to 30% sucrose. After the 3D structures sink, they were

735 embedded in O.C.T. (Sakura, Tokyo, Japan) and sliced in a cryostat (20 μ m slices). Following air
736 dry, the slides containing the sliced samples were permeabilized/blocked with 0.1% triton X-100
737 and 3% FBS in PBS for 2 hours at room temperature, and incubated with primary antibodies
738 overnight at 4°C. Primary antibodies used in this study were: mouse anti-Nestin, Abcam
739 (Cambridge, UK) ab22035, 1:250; rat anti-CTIP2, Abcam ab18465, 1:500; rabbit anti-SATB2,
740 Abcam ab34735, 1:200; chicken anti-MAP2, Abcam ab5392, 1:2000; rabbit anti-Synapsin1, EMD-
741 Millipore AB1543P, 1:500; mouse anti-NeuN, EMD-Millipore MAB377, 1:500; rabbit anti-Ki67,
742 Abcam ab15580, 1:1000; rabbit anti-SOX2, Cell Signaling Technology 2748, 1:500; rabbit anti-
743 GFAP, DAKO Z033429, 1:1000; rabbit anti-TBR1, Abcam ab31940, 1:500; rabbit anti-TBR2,
744 Abcam ab23345, 1:500; rabbit anti-beta-catenin, Abcam E247, 1:200; mouse anti-GABA, Abcam
745 ab86186, 1:200; rabbit anti-PROX1, Abcam ab101651, 1:250. Next, the slices were washed with
746 PBS and incubated with secondary antibodies (Alexa Fluor 488-, 555- and 647-conjugated
747 antibodies, Life Technologies, 1:1000) for 2 hours at room temperature. The nuclei were stained
748 using DAPI solution (1 μ g/mL). The slides were mounted using ProLong Gold antifade reagent
749 and analyzed under a fluorescence microscope (Axio Observer Apotome, Zeiss).

750

751 **Synaptic puncta quantification.** Pre-synaptic Syn1+ puncta were quantified after 3D
752 reconstruction of z-stacks of random images from randomly selected regions of all lines and from
753 two independent experiments. Only puncta overlapping MAP2-positive processes were scored.

754

755 **Immuno-gold electron microscopy (EM).** Immuno-gold EM was performed at the CMM Electron
756 Microscopy Facility at University of California San Diego. Four-month-old organoids were fixed
757 using 4% paraformaldehyde in 0.1M phosphate buffer (pH 7.4). Fixed cells were pelleted and
758 washed with 0.15 M glycine/phosphate buffer, embedded in 10% gelatin/phosphate buffer and
759 infused with 2.3 M sucrose/phosphate buffer. Blocks of cells with 1 mm³ were mounted onto
760 specimen holders and snap frozen in liquid nitrogen. Ultracryomicrotomy was carried out at –

761 100°C on a Leica Ultracut UCT with EM FCS cryoattachment (Leica, Bannockburn, IL) using a
762 Diatome diamond knife (Diatome US, Hatfield, PA). 80 to 90 nm frozen sections were picked up
763 with a 1:1 mixture of 2.3 M sucrose and 2% methyl cellulose (15cp) and transferred onto Formvar
764 and carbon-coated copper grids. Briefly, grids were placed on 2% gelatin at 37 °C for 20 min,
765 rinsed with 0.15 M glycine/PBS and the sections were blocked using 1% cold water fish-skin
766 gelatin. Grids were analyzed using a Tecnai G2 Spirit BioTWIN transmission electron microscope
767 equipped with an Eagle 4k HS digital camera (FEI, Hillsboro, OR).

768

769 **Targeted single-cell qRT-PCR and analysis.** Specific target amplification was performed in
770 individual dissociated cortical organoids using C1 Single-Cell and BioMark HD Systems (Fluidigm,
771 San Francisco, CA, USA), according to the manufacturer's protocol and as previously described
772 (Thanathom *et al.*, 2016). Briefly, cortical organoids were mechanically dissociated after 30
773 minutes of incubation in Accumax (Innovative Cell Technologies, San Diego, CA, USA) at 37 °C
774 under rotation. After passing through 100-µm and 40-µm strainers, cells were centrifuged and
775 resuspended in Media2 (see *Generation of cortical organoids*). Single cortical cells were captured
776 on a C1 medium chip and cell viability was assessed using a LIVE/DEAD Cell Viability/Cytotoxicity
777 kit (Life Technologies). The targeted single-cell qPCR was performed using DELTAgene primer
778 pairs in the 96.96 Dynamic Array IFC chip. The results were analyzed using Fluidigm Real-time
779 PCR Analysis Software and Singular Analysis Toolset 3.0 (Fluidigm).

780

781 **10X genomics single-cell and analysis.** After organoid dissociation, single cells were processed
782 through the Chromium Single Cell Gene Expression Solution using the Chromium Single Cell 3'
783 Gel Bead, Chip and Library Kits v2 (10X Genomics, Pleasanton) as per the manufacturer's
784 protocol. In brief, single cells were resuspended in 0.1% BSA in PBS. Five thousand cells were
785 added to each channel with an average recovery rate of 1,746 cells. The cells were then
786 partitioned into Gel Beads in Emulsion in the Chromium instrument, where cell lysis and barcoded

787 reverse transcription of RNA occurred, followed by amplification, shearing and 5' adaptor and
788 sample index attachment. Libraries were sequenced on an Illumina HiSeq 2500. De-multiplexing,
789 alignment to the hg19 transcriptome and unique molecular identifier (UMI)-collapsing were
790 performed using the Cellranger toolkit (version 2.0.1) provided by 10X Genomics. A total of 3,491
791 cells with approximately 53,000 reads per cell were processed. Analysis of output digital gene
792 expression matrices was performed using the Seurat R package. Matrices for replicates were
793 merged with the MergeSeurat function and all genes that were not detected in at least 5% of all
794 single cells were discarded, leaving 10,594 genes for further analyses. Cells with fewer than 600
795 or more than 8,000 expressed genes as well as cells with more than 50,000 UMIs or 0.1%
796 mitochondrial expressed genes were removed from the analysis. Data were log normalized and
797 scaled to 10,000 transcripts per cell. Variable genes were identified with the FindVariableGenes
798 function. Principal components were evaluated for statistically significant gene expression signals
799 using the JackStraw function. PCA was carried out, and the top 36 principal components were
800 retained. With these principal components, t-SNE was applied with the RunTSNE function to
801 visualize the cells in two dimensions and identified distinct cell clusters with the FindClusters
802 function with resolution = 0.30. Differential expression to identify cluster markers was performed
803 using the FindAllMarkers function.

804

805 **Data availability.** All data and/or analyses generated during the current study are available from
806 the corresponding author upon reasonable request. Single-cell RNA sequencing data that support
807 the findings of this study have been deposited at NCBI GEO: GSE113089.

808 **Multi-electrode array (MEA) recording.** Six-week-old cortical organoids were plated per well in
809 12-well MEA plates (Axion Biosystems, Atlanta, GA, USA). Each well contains 64 platinum
810 microelectrodes with 30 μm of diameter spaced by 200 μm , yielding a total of 512 channels. The
811 plate was previously coated with 100 $\mu\text{g}/\text{mL}$ poly-L-ornithine and 10 $\mu\text{g}/\text{ml}$ laminin, and we
812 performed four independent experiments in duplicates. Cells were fed twice a week and

813 measurements were collected 24 hours after the medium was changed, once a week, starting at
814 two weeks after plating (8 weeks of organoid differentiation). Recordings were performed using a
815 Maestro MEA system and AxIS Software Spontaneous Neural Configuration (Axion Biosystems)
816 with a customized script for band-pass filter (0.1-Hz and 5-kHz cutoff frequencies). Spikes were
817 detected with AxIS software using an adaptive threshold crossing set to 5.5 times the standard
818 deviation of the estimated noise for each electrode (channel). The plate was first allowed to rest
819 for three minutes in the Maestro device, and then four minutes of data were recorded. For the
820 MEA analysis, the electrodes that detected at least 5 spikes/min were classified as active
821 electrodes using Axion Biosystems' Neural Metrics Tool. Bursts were identified in the data
822 recorded from each individual electrode using an inter-spike interval (ISI) threshold requiring a
823 minimum number of 5 spikes with a maximum ISI of 100 ms. A minimum of 10 spikes under the
824 same ISI with a minimum of 25% active electrodes were required for network bursts in the well.
825 The synchrony index was calculated using a cross-correlogram synchrony window of 20 ms.
826 Bright-field images were captured from each well to assess for neural density and electrode
827 coverage over time.

828

829 **Custom MEA analysis.** Custom MEA analysis and neonatal EEG/organoid LFP regression
830 model can be found in: <https://github.com/voytekresearch/OscillatoryOrganoids>. Raw MEA
831 recordings were converted to *.mat* files using Axion-provided functions and analyzed offline using
832 custom MATLAB functions and scripts. Local field potential signals (LFP) from each of the 64
833 electrodes were generated by low-pass filtering (FIR filter) and downsampling raw signals from
834 12,500 Hz to 1,000 Hz (*resample.m*). Multi-unit spikes were detected as follows: each channel
835 was first referenced to the well median (64 channels). The median was used instead of the mean
836 to avoid biasing the reference during high firing rate periods. Next, the re-referenced signal was
837 bandpass filtered for 300-3,000 Hz with a 3rd-order Butterworth filter (*butter.m*). The spike
838 threshold was set to be 5.5 standard deviations, where the standard deviation was estimated as

839 previously described (Quiroga *et al.*, 2004) to avoid biasing the threshold for channels with high
840 firing rates (thus an artificially high threshold). Spike timestamps were taken as the peak time
841 after the absolute value of the signal crossed the threshold, but at least 1 ms from another spike
842 (*findpeaks.m*). Spike timestamps were then converted into binary vectors (1 ms bin size), summed
843 across 64 channels, and smoothed (*conv.m*) with a normalized 100-point Gaussian window
844 (*gausswin.m*) to create a population spiking vector for each MEA well. Note that spikes from each
845 channel do not represent putative single-unit action potentials, as the spatial resolution of MEA
846 electrodes were too sparse. Multi-unit spiking were not sorted since total population spiking (of
847 well) was submitted for further analysis, rather than individual spike trains.

848

849 **Network event analysis.** A network event was detected when population spiking was i) greater
850 than 80% of the maximum spiking value over the length of the recording; ii) at least 1 spike/s; and
851 iii) 1 second away from any other network events. The first peak after all 3 criteria was satisfied
852 was marked as $t = 0$, and the window of data from 0.5 s before to 2.5 s after the peak was collected
853 as the network event. Nearly all spiking channels experienced a significant firing rate increase
854 during network events. LFP data from all 64 channels from the same timeframe were also
855 collected for analysis. All events from different MEA wells obtained on the same recording day
856 were aggregated for statistical analysis and plotting. Subpeaks within an event were identified
857 using *findpeaks.m*, where a subpeak must satisfy the following: i) peak height of at least 25% of
858 the first peak; ii) peak width of at least 50 ms; iii) at least 200 ms away from the previous peak;
859 and iv) peak prominence of 1 over Peak 1 height. Subpeak time and the height relative to the
860 initial peak were recorded. The inter-event interval coefficient of variation (IEI CV) was calculated
861 as the standard deviation of the inter-event interval divided by its mean, where IEI is the time
862 between consecutive network events within the same MEA well. Event temporal correlation was
863 calculated as the mean Pearson correlation coefficient of population spiking vector during each
864 network event with every other network event in the same MEA well across a single recording

865 session. Event spatial correlation was calculated as the mean Pearson correlation coefficient
866 between all pairs of 64 LFP channels during each 3-s network event.

867

868 **Oscillatory spectral power analysis.** Power spectral density (PSD) estimates were computed
869 using Welch's method (*pwelch.m*), with a window length of 2 s and overlap of 1 s. Oscillatory
870 power was defined as peaks in the PSD above the aperiodic $1/f$ power law decay. Thus, for each
871 channel, a straight line was fit over the PSD in double-log space between 0.5-20 Hz using robust
872 fit (*robustfit.m*), and oscillatory power was computed as the difference between the mean log PSD
873 power and the mean log fitted power (baseline), over 2.5-4.5 Hz.

874

875 **Regression models.** For analysis in Figure 2F, G and S7C, F, G, we fit regression models
876 (*LinearModel.fit*, *MATLAB*) using organoid age (in days) as input and electrophysiological features
877 as output. Order-1 (linear) models were fit for Figure 2G and and S7C, G, and order-2 (quadratic)
878 models were fit for Figure 2F, 3C and Figure S7F. Reported R^2 and p values are model statistics
879 over the entire dataset. All events from different MEA wells on the same recording day were
880 aggregated as samples drawn from the same distribution. To predict culture age, we used 3
881 electrophysiological features as input: event latency, event peak spiking, and oscillatory power;
882 and their square roots to account for the nonlinear inverted-U features. These were used to build
883 a regression model. Within-well models were fit over all data points of the same well, and
884 goodness-of-fit was reported as the model R^2 and the RMSE. Across-well models were trained
885 and evaluated using leave-1-out cross-validation, and goodness-of-fit is reported as the R^2 and
886 the RMSE computed over the validation set, not the training set.

887

888 **Phase Amplitude Coupling (PAC).** LFP data from all 64 channels of each well was first
889 lowpass/bandpass filtered (*eegfilt.m*, *EEGLAB*) for delta (0-4 Hz) and high-frequency, broadband
890 gamma (100-400 Hz) activity. Delta phase was extracted by taking the phase angle of the

891 bandpassed delta signal Hilbert transform (*hilbert.m*, *angle.m*), while gamma power was extracted
892 by taking the squared magnitude of the filtered gamma. Gamma power was smoothed with the
893 same delta-band filter for display purposes, but not for subsequent analysis. Note that analysis
894 was done for 100-200 Hz and 200-400 Hz separately, as LFP spectrum follows an inverse power
895 law ($1/f$), and grouping a wide frequency band (100-400 Hz) together will bias power estimates
896 towards lower frequency limits (~ 100 Hz). To compute PAC, instantaneous delta phase was
897 binned into 20 equidistant bins between $-\pi$ and π , and gamma power was sorted based on the
898 corresponding delta phase at the same sample time and averaged across the same phase bin.
899 This procedure was performed separately for event and non-event indices, where event indices
900 are the same 3-s windows as described above in *Network Event Analysis*. Modulation Index was
901 computed as the Kullback-Leibler divergence between the sum-normalized distribution of gamma
902 power across phase bins and a uniform distribution (Tort et al., 2010). Figure 3C presents well-
903 averaged MI across all 64 channels. For visualization in Figure 3b, the binned gamma vector for
904 each channel was circularly shifted such that the phase of maximum gamma power was $-\pi$.

905

906 **Pharmacology.** The pharmacological manipulation was performed using the following drugs: 10
907 μM bicuculline, 50 μM muscimol, 20 μM CNQX, 20 μM AP5, 25 μM baclofen and 1 μM TTX. In
908 this assessment, baseline recordings were obtained immediately before and 15 min after the
909 addition of the compound. Three washes with PBS for total removal of the drug were performed
910 in washout experiments; fresh media was added and another recording was conducted after 2
911 hours.

912

913 **Preterm neonatal EEG.** A preterm neonatal EEG dataset was obtained elsewhere (Stevenson
914 et al., 2017). Raw recordings were not available due to patient confidentiality concerns. The
915 dataset includes 567 recordings from 39 preterm neonates (24-38 weeks old conception age),
916 consisting of 23 EEG features computed from the entirety of each recording, as well as during

917 “low-activity periods” (46 features in total), and the post-conception age in weeks.

918

919 **Neonate-organoid age prediction model.** To compare the developmental trajectory of cortical
920 organoids and the preterm human brain, we trained an Elastic Net (L1- and L2- regularized)
921 regression model on only the preterm neonatal EEG features and used that model (with all
922 parameters held the same) to generate an equivalent organoid “brain-age” for each recording
923 time point over 40 weeks in culture. Specifically, the training dataset consists of a subset of the
924 preterm EEG data; of the 46 included features, we discarded all “low-activity-period” features
925 (Lisman, 1997) since there was no equivalent period for organoid recordings, as well as features
926 for which we could not sensibly compute from organoid LFPs, such as interhemispheric
927 synchrony. This selection was done *a priori*, and 13 features remained, including 4 features for
928 relative spectral power in distinct frequency bands, which were further discarded due to
929 frequency-dependent filtering properties of the skull and difference in spatial integration of
930 currents in macroscopic EEG electrodes compared to microscopic planar MEA electrodes. The
931 remaining 9 features correspond to aspects of spontaneous activity transient (SAT) timing, such
932 as SATs per hour and SAT duration, which were similarly computed on organoid LFPs after
933 network event detection described earlier (see Supplementary Table 2 for a full list of included
934 and rejected features). This latter organoid LFP test dataset was never seen by the regression
935 model until prediction time. Training was performed using scikit-learn linear model module
936 [(ElasticNetCV (Pedregosa et al., 2011))], with K-Group shuffle split cross-validation on
937 regularization hyperparameters, where K = 25% of groups, N = 200 shuffles. In other words, we
938 found the best regularized linear model possible for predicting the conception age of preterm
939 neonates using those 9 precomputed EEG features. This model was directly applied on organoid
940 LFP features to determine the corresponding “brain age” of the organoids during 40 weeks in
941 culture. 1-sample *t*-tests were performed from every time point to test whether the mean predicted
942 “brain age” was significantly different from the organoid culture age.

943

944 **Resampled feature correlation.** We computed Pearson's correlation coefficient between
945 neonate age and each of the 9 EEG features, after a leave-K-groups-out resampling procedure
946 N times, where K is the number of neonates from whom all recordings were left out in computing
947 the correlation (50% of all neonates, resampling N = 100). An identical procedure was performed
948 to compute the correlation between organoid culture age and LFP features (K = 4 out of 8, 50%,
949 N = 100). Mean and standard deviation were then computed over all resampled draws in order to
950 compare between organoid LFP and neonatal EEG.

951

952 **Statistical analysis.** Data are presented as mean \pm s.e.m., unless otherwise indicated, and it was
953 obtained from different samples. No statistical method was used to predetermine the sample size,
954 and no adjustments were made for multiple comparisons. The statistical analyses were performed
955 using Prism software (GraphPad, San Diego, CA, USA). Student's *t*-test, Mann–Whitney-test, or
956 ANOVA with post hoc tests were used as indicated. Significance was defined as $P < 0.05$ (*), $P <$
957 0.01 (**), or $P < 0.001$ (***). Blinding was used for comparing affected and control samples.

958

959 **SUPPLEMENTARY FIGURE LEGENDS**

960 **Supplementary Figure 1. Cellular and molecular characterization of human cortical**

961 **organoids.** (A) Schematic of the protocol used to generate cortical organoids. Scale bar, 200 μm .

962 (B) Reproducibility of organoid size at 2 months of maturation ($n = 20$ independent experiment, 7

963 different cell lines). (C) Organoids are composed of a proliferative region surrounded by

964 intermediate progenitor cells, cortical and GABA⁺ neurons. Scale bar, 50 μm . (D) Principal

965 component analysis (PCA) of cells projected onto the first two components. Overlaid populations

966 of 2- and 10-month-old cortical organoids are compared to 2-month-old 2D monolayer neurons.

967 All timelines for this and the subsequent experiments consider the iPSC stage as day 0 ($n = 2$

968 independent cell lines for each cortical culture; $n = 3$ for 2D monolayer neurons). (E-F) Violin plots

969 illustrate the differences in single-cell expression of target genes in cortical organoids and 2D

970 neurons. (G-H) Unsupervised hierarchical clustering single-cell analysis. Genes were clustered

971 using the Pearson correlation method and cells were clustered using the Euclidean method.

972

973 **Supplementary Figure 2. Reproducibility and single-cell characterization.** (A) Schematic

974 showing the single-cell approach performed to assess reproducibility of organoid generation using

975 two control iPSC lines. (B) *t*SNE plot of single-cell mRNA sequencing data from 6-month-old

976 organoids color-coded by replicate. (C) Split Dot Plot depicting the correlation between expression

977 patterns of representative markers and cell populations identified within the dataset. The size of

978 the dots represents the percentage of cells expressing a given gene, while the intensity of the

979 color denotes the average expression level (grey, low expression; red/blue, high expression). (D)

980 Population ratio of each cluster by replicate.

981

982 **Supplementary Figure 3. Cell diversity in cortical organoids.** Violin and *t*SNE plots of selected

983 genes depicting the proportion of cells contributing to each cluster. For the violin plots, the dot

984 denotes a cell while colors correspond to their cluster identity. The *t*SNE plots show the

985 contribution of an individual cell-type marker within each cluster (red denotes higher expression).

986

987 **Supplementary Figure 4. Cell type identity of 6-month-old cortical organoids.** Heat map

988 reports scaled expression of discriminative gene sets for clusters defined in Figure 1h with AUC

989 cutoff ≥ 0.80 . Color scheme is based on z-score distribution from -2.5 (blue) to 2.5 (red). For gene

990 lists and AUC values see Supplementary Table 1.

991

992 **Supplementary Figure 5. Long-term MEA network activity.** (A) Representative bright-field

993 images of cortical organoids over time on the MEA plate. (B) Schematic representation of the

994 electrical activity features analyzed from the MEA recordings. Each bar represents a spike; and

995 a spike cluster (in blue) represents a burst. Bursts occurring at the same time in different channels

996 characterize a network burst. The synchrony index is based on the cross-correlogram and

997 represents a measure of similarity between two spike trains. (C) Temporal evolution of network

998 activity characterized by different parameters. (D) Raster plots illustrating the development of

999 network activity. (E) Consistent and reproducible development of electrical activity in cortical

1000 organoids over time. The data are shown as mean \pm s.e.m ($n = 8$, independent experiments

1001 performed in duplicates using two clones of a control iPSC line).

1002

1003 **Supplementary Figure 6. MEA electrical activity comparison of cortical organoids with**

1004 **available published data from iPSC-derived neurons, organoids, rodent primary cultures**

1005 **and primate models.** (A) Long-term network activity of our cortical organoids is shown for

1006 individual wells. Comparison of network activity between cortical organoids and iPSC-derived

1007 cortical neurons (B), rodent primary neuronal cultures and primate models (C). The data shown

1008 in B and C for cortical organoids are presented as mean \pm s.e.m. ($n = 8$, independent experiments

1009 performed in duplicates) (Amin *et al.*, 2016; Bardy *et al.*, 2015; Barz *et al.*, 2017; Brown *et al.*,

1010 2016; Cesca *et al.*, 2015; Clements *et al.*, 2016; Cotterill *et al.*, 2016; Harrill *et al.*, 2015; Marchetto
1011 *et al.*, 2016; McSweeney *et al.*, 2016; Odawara *et al.*, 2014, 2016; Roy *et al.*, 2016; Strickland *et*
1012 *al.*, 2016; Tukker *et al.*, 2016; Uesaka *et al.*, 2007; Vessoni *et al.*, 2016; Wallace *et al.*, 2015; Xu
1013 *et al.*, 2017; Yang *et al.*, 2016).

1014

1015 **Supplementary Figure 7. Extended characterization of network electrophysiology.** (A)

1016 Spikes detected on 9 channels. Black traces represent single spikes, blue and red traces
1017 represent the average of positive and negative spikes, respectively. Spike trains are not sorted
1018 for their polarity in the subsequent analyses, as total population spiking is the main feature of
1019 interest. (B) Representative oscillatory network events. Each overlapping trace represents a
1020 single occurrence of an event recorded on the same channel. LFP polarity of events differs
1021 between channels due to the spatial configuration of cells around the electrode. (C) Event onset
1022 peak (Peak 1) increases in amplitude until 30 weeks, while (D) subpeak amplitude continues to
1023 increase (for the 2nd-4th peak) throughout development. (E) Subsequent peaks occur with a
1024 consistent latency of ~400 ms after the previous peak, particularly for Peak 3 and 4. (F) Temporal
1025 similarity of network events during the 3-s window is high at early time points, but decreases with
1026 development, acquiring more variable dynamics within an event. (G) Temporal similarity of
1027 network events during the 3-s window is high at early time points, but decreases with
1028 development, acquiring more variable dynamics within an event. The data showed in C, F and G
1029 are presented as mean \pm s.e.m., linear (C, G) or quadratic (F) model regression.

1030

1031 **Supplementary Figure 8. MEA recording from 3-month-old neurospheres.** (A) Comparison

1032 of the protocol for neurosphere and cortical organoid generation. (B) Network-wide giant
1033 depolarizing potentials occur at a similar rate to those found in organoids recordings, and visible
1034 perturbations are observed in the LFP trace. However, the network recruitment in neurospheres
1035 is lower than in organoids (less than 8 spikes/s), and events have significantly shorter duration.

1036 No coherent low-frequency depolarizations are observed in filtered LFP events (C).

1037 **Supplementary Figure 9. MECP2-KO cell line characterization.** (A) Schematic overview of the
1038 *MECP2* locus in iPSCs derived from fibroblasts of a male patient (Q83X), and CRISPR/Cas9
1039 induced *MECP2* mutation in an embryonic stem cell line (K82fs, H9 ESC). Q83X cell line
1040 characterization is shown elsewhere (Zhang *et al.*, 2016). DNA sequence chromatogram shows
1041 the nucleotide deletion in the *MECP2* gene leading to a frameshift mutation (K82fs) and a
1042 predicted premature stop-codon at the end of exon 3 (asterisk). The WT82 and WT83 were used
1043 as controls. The Q83X and K82fs do not express MECP2 protein. Blue line represents the guide
1044 RNA target locus. (B) Gel images showing Surveyor nuclease assay of genomic DNA extracted
1045 from FACs sorted H9 ESC. Expected PCR products were 278 bp and 220 bp. (C) Exome
1046 sequencing analysis to evaluate CRISPR off-target mutations. Numbers indicate the amount of
1047 reads across the lines. Off-target gene mutations induced by *MECP2* CRISPR/Cas9 are shown
1048 in the lower table. (D) Isogenic pairs of *MECP2*-mutant and control cell line colonies showing the
1049 expression of the pluripotency marker Nanog. Scale bar, 100 μm . (E) Eosin and Hematoxylin
1050 stains of teratomas showing the presence of all three germ layers. Scale bar, 200 μm . (F) Western
1051 blot of the isogenic pluripotent stem cells showing the absence of MECP2 in the mutant line. (G)
1052 Karyotypes of cell lines displaying no chromosomal abnormality. (H and I) Expression of
1053 pluripotency markers and *MECP2* by qPCR. GAPDH was used as housekeeping gene.

1054

1055 **Supplementary Figure 10. Network activity in cortical organoids mimics oscillatory**
1056 **features in the developing human brain.** (A) Spectral representation of time series data from a
1057 6-month-old cortical organoid, demonstrating oscillatory phenomenon. Spectrogram (left) of
1058 organoid LFP shows bursts of activity localized at low frequencies, while power spectral density
1059 (PSD, right) displays canonical $1/f$ power law decay and a narrow oscillatory peak at 3 Hz. (B)
1060 Comparison of 9 preterm neonate EEG and cortical organoid features over time. For included
1061 EEG features, see Table S2. (C) Distributions of resampled Pearson correlation coefficients

1062 between feature and age for preterm neonate and organoid.

1063

1064 **SUPPLEMENTARY TABLES**

1065

1066 **Supplementary Table 1. Top expressed genes of each cell cluster.**

Cluster	Gene	myAUC	avg_diff	power	avg_logFC	pct.1	pct.2	p_val_adj
Cortical neurons	SOX11	0.889	1.29996	0.778	1.29996	0.996	0.864	NA
Cortical neurons	NEUROD2	0.886	1.366603	0.772	1.366603	0.944	0.382	NA
Cortical neurons	GPM6A	0.885	1.12235	0.77	1.12235	0.992	0.679	NA
Cortical neurons	SOX4	0.879	0.985057	0.758	0.985057	1	0.965	NA
Cortical neurons	MLLT11	0.856	0.916514	0.712	0.916514	0.998	0.869	NA
Cortical neurons	CCNI	0.843	0.707003	0.686	0.707003	1	0.994	NA
Cortical neurons	SLA	0.833	1.424488	0.666	1.424488	0.821	0.303	NA
Cortical neurons	MARCKSL1	0.832	0.578678	0.664	0.578678	0.999	0.981	NA
Cortical neurons	DCX	0.806	0.81224	0.612	0.81224	0.969	0.576	NA
Progenitors	NES	0.976	1.785855	0.952	1.785855	0.997	0.303	NA
Progenitors	ANXA2	0.972	2.407607	0.944	2.407607	0.976	0.149	NA
Progenitors	GYPC	0.963	1.587675	0.926	1.587675	0.954	0.065	NA
Progenitors	SPARC	0.958	1.745727	0.916	1.745727	0.978	0.24	NA
Progenitors	SDC2	0.944	1.388854	0.888	1.388854	0.924	0.08	NA
Progenitors	CRABP2	0.942	1.564316	0.884	1.564316	0.939	0.11	NA
Progenitors	NTRK2	0.941	1.61904	0.882	1.61904	0.912	0.057	NA
Progenitors	CCND1	0.941	1.505771	0.882	1.505771	0.909	0.046	NA
Progenitors	LGALS1	0.938	2.0633	0.876	2.0633	0.94	0.17	NA
Progenitors	SERF2	0.934	0.95158	0.868	0.95158	1	0.903	NA
Progenitors	MDK	0.933	1.279235	0.866	1.279235	0.996	0.832	NA
Progenitors	VGLL3	0.931	1.237999	0.862	1.237999	0.887	0.032	NA
Progenitors	S100A13	0.917	1.839522	0.834	1.839522	0.893	0.12	NA
Progenitors	PDLIM7	0.916	1.185298	0.832	1.185298	0.94	0.25	NA

Progenitors	ANXA5	0.902	1.221643	0.804	1.221643	0.926	0.184	NA
Progenitors	PRSS23	0.901	1.501512	0.802	1.501512	0.836	0.06	NA
Progenitors	RPL41	0.897	0.625131	0.794	0.625131	1	0.999	NA
Progenitors	NPC2	0.895	1.182853	0.79	1.182853	0.951	0.407	NA
Progenitors	SEC11A	0.894	0.828695	0.788	0.828695	0.98	0.64	NA
Progenitors	PRDX6	0.892	0.981071	0.784	0.981071	0.98	0.555	NA
Progenitors	TPM1	0.887	1.731952	0.774	1.731952	0.938	0.518	NA
Progenitors	RHOC	0.887	0.962424	0.774	0.962424	0.907	0.206	NA
Progenitors	NEAT1	0.883	1.352256	0.766	1.352256	0.948	0.285	NA
Progenitors	RPL12	0.882	0.706881	0.764	0.706881	0.999	0.992	NA
Progenitors	RPL7A	0.881	0.613375	0.762	0.613375	1	0.997	NA
Progenitors	EEF1A1	0.879	0.651914	0.758	0.651914	1	1	NA
Progenitors	RPL28	0.876	0.592999	0.752	0.592999	1	0.995	NA
Progenitors	RPS6	0.871	0.711767	0.742	0.711767	0.997	0.994	NA
Progenitors	RPL23A	0.867	0.568383	0.734	0.568383	0.999	0.994	NA
Progenitors	TIMP1	0.865	0.772749	0.73	0.772749	0.895	0.173	NA
Progenitors	RPL8	0.864	0.572428	0.728	0.572428	0.999	0.997	NA
Progenitors	METRNL	0.863	0.835332	0.726	0.835332	0.907	0.229	NA
Progenitors	WLS	0.859	0.916782	0.718	0.916782	0.736	0.023	NA
Progenitors	RPL27A	0.858	0.534803	0.716	0.534803	1	0.998	NA
Progenitors	CTGF	0.857	1.335629	0.714	1.335629	0.727	0.017	NA
Progenitors	RCN1	0.857	0.806462	0.714	0.806462	0.967	0.377	NA
Progenitors	PFN1	0.857	0.738107	0.714	0.738107	0.99	0.844	NA
Progenitors	PMP22	0.855	1.601169	0.71	1.601169	0.778	0.101	NA
Progenitors	ITGB8	0.855	1.138802	0.71	1.138802	0.868	0.201	NA
Progenitors	SERPINH1	0.854	0.713982	0.708	0.713982	0.846	0.143	NA
Progenitors	VIM	0.853	1.146246	0.706	1.146246	1	0.77	NA
Progenitors	NME4	0.852	0.813408	0.704	0.813408	0.945	0.457	NA
Progenitors	RPS7	0.852	0.558045	0.704	0.558045	0.999	0.997	NA
Progenitors	MYL12A	0.85	0.739735	0.7	0.739735	0.84	0.157	NA
Progenitors	RPS20	0.849	0.558658	0.698	0.558658	1	0.991	NA

Progenitors	RPS2	0.848	0.524557	0.696	0.524557	0.999	1	NA
Progenitors	RPLP1	0.848	0.514123	0.696	0.514123	1	0.998	NA
Progenitors	RAB13	0.846	0.808108	0.692	0.808108	0.86	0.204	NA
Progenitors	TUBB6	0.845	0.757197	0.69	0.757197	0.806	0.121	NA
Progenitors	CRNDE	0.843	0.802352	0.686	0.802352	0.954	0.472	NA
Progenitors	TTYH1	0.84	0.971997	0.68	0.971997	0.963	0.416	NA
Progenitors	RPL23	0.84	0.546833	0.68	0.546833	1	0.997	NA
Progenitors	RPS19	0.84	0.516859	0.68	0.516859	1	1	NA
Progenitors	RPL29	0.84	0.464037	0.68	0.464037	1	0.997	NA
Progenitors	RPS14	0.839	0.462974	0.678	0.462974	1	0.999	NA
Progenitors	RPL3	0.838	0.497988	0.676	0.497988	1	0.998	NA
Progenitors	SLC25A6	0.835	0.71474	0.67	0.71474	0.995	0.891	NA
Progenitors	SPATS2L	0.831	0.9606	0.662	0.9606	0.811	0.193	NA
Progenitors	QPRT	0.83	0.651751	0.66	0.651751	0.855	0.198	NA
Progenitors	RPL35	0.83	0.470972	0.66	0.470972	0.999	0.993	NA
Progenitors	RPS18	0.828	0.49256	0.656	0.49256	1	1	NA
Progenitors	CLIC1	0.827	0.723496	0.654	0.723496	0.937	0.427	NA
Progenitors	RPS3	0.827	0.526597	0.654	0.526597	1	0.997	NA
Progenitors	RPL10A	0.827	0.523565	0.654	0.523565	1	0.994	NA
Progenitors	RPS28	0.825	0.506021	0.65	0.506021	1	0.993	NA
Progenitors	CD63	0.824	0.710828	0.648	0.710828	0.991	0.76	NA
Progenitors	PDPN	0.824	0.65191	0.648	0.65191	0.699	0.046	NA
Progenitors	ACTG1	0.824	0.488252	0.648	0.488252	1	1	NA
Progenitors	CCNG1	0.823	0.727443	0.646	0.727443	0.924	0.38	NA
Progenitors	CD99	0.82	0.68859	0.64	0.68859	0.953	0.405	NA
Progenitors	B2M	0.817	0.787786	0.634	0.787786	0.947	0.392	NA
Progenitors	CHCHD10	0.817	0.645222	0.634	0.645222	0.84	0.211	NA
Progenitors	RPLP0	0.817	0.469741	0.634	0.469741	1	0.997	NA
Progenitors	RPS27L	0.816	0.744701	0.632	0.744701	0.995	0.664	NA
Progenitors	COL1A2	0.815	0.896012	0.63	0.896012	0.647	0.019	NA
Progenitors	PFN2	0.815	0.622861	0.63	0.622861	0.991	0.763	NA

Progenitors	UBB	0.813	0.783749	0.626	0.783749	0.978	0.588	NA
Progenitors	RPL37	0.813	0.465752	0.626	0.465752	1	0.995	NA
Progenitors	CRABP1	0.811	1.087669	0.622	1.087669	0.737	0.133	NA
Progenitors	RPL7	0.811	0.467728	0.622	0.467728	1	0.998	NA
Progenitors	FSTL1	0.81	0.761788	0.62	0.761788	0.737	0.123	NA
Progenitors	RPL36	0.81	0.434708	0.62	0.434708	1	0.992	NA
Progenitors	RPL19	0.81	0.401045	0.62	0.401045	1	1	NA
Progenitors	FGFR1	0.809	0.608769	0.618	0.608769	0.839	0.204	NA
Progenitors	ENO1	0.808	0.582772	0.616	0.582772	0.996	0.869	NA
Progenitors	RPS15	0.806	0.381154	0.612	0.381154	1	0.999	NA
Progenitors	MYL6	0.805	0.530039	0.61	0.530039	1	0.986	NA
Progenitors	GSTP1	0.804	0.634369	0.608	0.634369	0.996	0.92	NA
Progenitors	PODXL	0.804	0.622402	0.608	0.622402	0.67	0.06	NA
Progenitors	CNN3	0.804	0.616921	0.608	0.616921	0.992	0.669	NA
Progenitors	GNG11	0.803	0.751478	0.606	0.751478	0.668	0.064	NA
Progenitors	RPS4Y1	0.803	0.680093	0.606	0.680093	0.963	0.62	NA
Progenitors	AHNAK	0.803	0.651782	0.606	0.651782	0.64	0.036	NA
Progenitors	CST3	0.802	0.645478	0.604	0.645478	0.963	0.567	NA
Progenitors	RPS23	0.801	0.419435	0.602	0.419435	1	0.998	NA
Progenitors	RPL13A	0.801	0.409875	0.602	0.409875	1	1	NA
Glia	SFRP1	0.94	2.001041	0.88	2.001041	0.952	0.385	NA
Glia	SOX2	0.909	1.356804	0.818	1.356804	0.946	0.321	NA
Glia	C1orf61	0.893	1.500525	0.786	1.500525	0.984	0.749	NA
Glia	FABP7	0.887	1.707591	0.774	1.707591	0.985	0.736	NA
Glia	SLC1A3	0.88	1.56662	0.76	1.56662	0.807	0.119	NA
Glia	SYNE2	0.876	1.218806	0.752	1.218806	0.919	0.445	NA
Glia	PAX6	0.871	1.251984	0.742	1.251984	0.83	0.186	NA
Glia	HMG3	0.866	0.91378	0.732	0.91378	0.978	0.849	NA
Glia	ID4	0.851	1.407158	0.702	1.407158	0.875	0.381	NA
Glia	MYO10	0.85	1.025069	0.7	1.025069	0.857	0.338	NA
Glia	DBI	0.842	1.242287	0.684	1.242287	0.958	0.709	NA

Glia	PTN	0.836	1.579917	0.672	1.579917	0.948	0.752	NA
Glia	QKI	0.83	0.909655	0.66	0.909655	0.891	0.502	NA
Glia	LINC01158	0.818	0.903364	0.636	0.903364	0.901	0.546	NA
Glia	ZFHX4	0.817	1.004117	0.634	1.004117	0.707	0.132	NA
Glia	HES1	0.812	1.171994	0.624	1.171994	0.718	0.17	NA
Glia	HMGB2	0.809	1.270445	0.618	1.270445	0.921	0.594	NA
Glia	LHX2	0.806	0.931067	0.612	0.931067	0.846	0.398	NA
Lower cortex	SNAP25	0.942	1.540645	0.884	1.540645	0.987	0.415	NA
Lower cortex	GRIA2	0.892	1.185847	0.784	1.185847	0.96	0.352	NA
Lower cortex	CNTNAP2	0.88	1.447084	0.76	1.447084	0.876	0.272	NA
Lower cortex	CELF4	0.863	1.071334	0.726	1.071334	0.886	0.265	NA
Lower cortex	NSG2	0.851	1.031537	0.702	1.031537	0.96	0.403	NA
Lower cortex	SYT1	0.85	0.985569	0.7	0.985569	0.983	0.61	NA
Lower cortex	YWHAH	0.841	0.785308	0.682	0.785308	0.973	0.805	NA
Lower cortex	SNCA	0.839	0.953942	0.678	0.953942	0.914	0.451	NA
Lower cortex	BASP1	0.838	0.734567	0.676	0.734567	1	0.943	NA
Lower cortex	DOK6	0.831	1.000188	0.662	1.000188	0.814	0.264	NA
Lower cortex	RTN1	0.823	0.898627	0.646	0.898627	0.985	0.519	NA
Lower cortex	RUNX1T1	0.82	0.94366	0.64	0.94366	0.852	0.281	NA
Lower cortex	FAM49A	0.817	0.920672	0.634	0.920672	0.821	0.28	NA
Lower cortex	MAP1B	0.817	0.603691	0.634	0.603691	1	0.995	NA
Lower cortex	SYT4	0.816	0.939245	0.632	0.939245	0.821	0.262	NA
Lower cortex	B3GALT2	0.815	1.017411	0.63	1.017411	0.757	0.2	NA
Lower cortex	GABRB2	0.815	0.991632	0.63	0.991632	0.675	0.062	NA
Lower cortex	LMO3	0.814	1.36195	0.628	1.36195	0.688	0.101	NA
Lower cortex	SCG3	0.811	0.757346	0.622	0.757346	0.939	0.415	NA
Lower cortex	UCHL1	0.809	0.66339	0.618	0.66339	0.99	0.906	NA
Lower cortex	VAMP2	0.809	0.606955	0.618	0.606955	0.994	0.939	NA
Lower cortex	TMEM161B-AS1	0.808	0.816917	0.616	0.816917	0.941	0.63	NA
Lower cortex	LY6H	0.806	0.807691	0.612	0.807691	0.88	0.34	NA
Lower cortex	MAPT	0.805	0.73704	0.61	0.73704	0.962	0.486	NA

Lower cortex	CDKN2D	0.802	0.762383	0.604	0.762383	0.878	0.4	NA
Lower cortex	RAB3A	0.801	0.697869	0.602	0.697869	0.924	0.413	NA
Upper cortex	MEF2C	0.954	2.051853	0.908	2.051853	0.986	0.369	NA
Upper cortex	STMN2	0.885	1.043931	0.77	1.043931	1	0.644	NA
Upper cortex	NSG2	0.883	1.126043	0.766	1.126043	1	0.441	NA
Upper cortex	ARPP21	0.88	1.115469	0.76	1.115469	0.883	0.189	NA
Upper cortex	STMN4	0.874	0.982886	0.748	0.982886	1	0.696	NA
Upper cortex	MAPT	0.87	0.908315	0.74	0.908315	1	0.518	NA
Upper cortex	GRIN2B	0.869	1.002716	0.738	1.002716	0.9	0.246	NA
Upper cortex	CALM1	0.868	0.733117	0.736	0.733117	1	0.988	NA
Upper cortex	NELL2	0.861	0.95751	0.722	0.95751	0.973	0.409	NA
Upper cortex	SCD5	0.855	0.913699	0.71	0.913699	0.931	0.478	NA
Upper cortex	SATB2	0.853	0.902036	0.706	0.902036	0.811	0.125	NA
Upper cortex	PKIA	0.849	0.808509	0.698	0.808509	0.952	0.445	NA
Upper cortex	MAP1B	0.849	0.669352	0.698	0.669352	1	0.995	NA
Upper cortex	INA	0.847	0.831367	0.694	0.831367	0.966	0.437	NA
Upper cortex	STMN1	0.845	0.783568	0.69	0.783568	1	0.979	NA
Upper cortex	NEUROD6	0.843	1.007963	0.686	1.007963	0.986	0.502	NA
Upper cortex	VAMP2	0.843	0.689091	0.686	0.689091	0.993	0.943	NA
Upper cortex	DOK5	0.841	0.93379	0.682	0.93379	0.935	0.559	NA
Upper cortex	RASL11B	0.841	0.930199	0.682	0.930199	0.821	0.209	NA
Upper cortex	SNCA	0.841	0.896556	0.682	0.896556	0.952	0.482	NA
Upper cortex	R3HDM1	0.84	0.924861	0.68	0.924861	0.89	0.386	NA
Upper cortex	TTC9B	0.84	0.868857	0.68	0.868857	0.959	0.435	NA
Upper cortex	RAC3	0.83	0.70783	0.66	0.70783	0.945	0.624	NA
Upper cortex	CXADR	0.827	0.785512	0.654	0.785512	0.993	0.719	NA
Upper cortex	HN1	0.827	0.602815	0.654	0.602815	1	0.961	NA
Upper cortex	CAMK2B	0.822	0.749623	0.644	0.749623	0.897	0.279	NA
Upper cortex	RTN1	0.819	0.807888	0.638	0.807888	1	0.553	NA
Upper cortex	CHL1	0.819	0.775621	0.638	0.775621	0.918	0.374	NA
Upper cortex	NSG1	0.818	0.708593	0.636	0.708593	0.997	0.528	NA

Upper cortex	TUBB2A	0.817	0.659235	0.634	0.659235	1	0.946	NA
Upper cortex	GABBR2	0.815	0.777596	0.63	0.777596	0.79	0.182	NA
Upper cortex	RBFOX2	0.814	0.677032	0.628	0.677032	0.99	0.662	NA
Upper cortex	CRMP1	0.813	0.666121	0.626	0.666121	0.979	0.79	NA
Upper cortex	GAP43	0.811	0.737576	0.622	0.737576	0.997	0.816	NA
Upper cortex	UCHL1	0.809	0.645161	0.618	0.645161	1	0.911	NA
Upper cortex	CDKN2D	0.808	0.694482	0.616	0.694482	0.935	0.43	NA
Upper cortex	NCAM1	0.805	0.694452	0.61	0.694452	0.955	0.551	NA
Upper cortex	MSRA	0.804	0.734229	0.608	0.734229	0.814	0.288	NA
Upper cortex	GPR85	0.801	0.76111	0.602	0.76111	0.766	0.189	NA
Upper cortex	DAAM1	0.801	0.628961	0.602	0.628961	0.993	0.776	NA
Other	ALDOA	0.917	1.757415	0.834	1.757415	0.963	0.838	NA
Other	EIF1	0.888	0.999198	0.776	0.999198	1	0.999	NA
Other	FTL	0.883	1.541462	0.766	1.541462	1	0.997	NA
Other	BNIP3	0.87	1.504624	0.74	1.504624	0.844	0.345	NA
Other	FAM162A	0.857	1.366057	0.714	1.366057	0.881	0.459	NA
Other	ARF4	0.848	1.242187	0.696	1.242187	0.889	0.715	NA
Other	ENO1	0.845	1.199331	0.69	1.199331	0.978	0.894	NA
Other	P4HA1	0.832	1.239505	0.664	1.239505	0.741	0.175	NA
Other	TRMT112	0.825	0.918451	0.65	0.918451	0.926	0.735	NA
Other	RPS13	0.822	0.756328	0.644	0.756328	0.993	0.998	NA
Other	TPT1	0.817	0.840456	0.634	0.840456	0.993	0.998	NA
Other	SEC61G	0.812	0.841716	0.624	0.841716	0.963	0.881	NA
Other	PGK1	0.809	1.333477	0.618	1.333477	0.881	0.803	NA
Other	GADD45A	0.802	1.332596	0.604	1.332596	0.741	0.3	NA
Other	ST13	0.801	0.866714	0.602	0.866714	0.963	0.878	NA
Neural crest	TAGLN3	0.922	1.681741	0.844	1.681741	1	0.686	NA
Neural crest	PBX3	0.917	1.457984	0.834	1.457984	0.878	0.154	NA
Neural crest	CRABP1	0.886	2.63702	0.772	2.63702	0.892	0.257	NA
Neural crest	MEG3	0.872	2.436136	0.744	2.436136	0.824	0.289	NA
Neural crest	ACTG1	0.851	0.573491	0.702	0.573491	1	1	NA

Neural crest	MIAT	0.82	1.008958	0.64	1.008958	0.932	0.671	NA
Neural crest	KCNQ1OT1	0.818	1.242528	0.636	1.242528	0.905	0.547	NA
Neural crest	NEAT1	0.806	0.991861	0.612	0.991861	0.865	0.427	NA
Neural crest	ELAVL2	0.806	0.728978	0.612	0.728978	0.932	0.464	NA
Neural crest	RGMB	0.804	1.190676	0.608	1.190676	0.703	0.168	NA

1067

1068

1069

1070

1071

1072

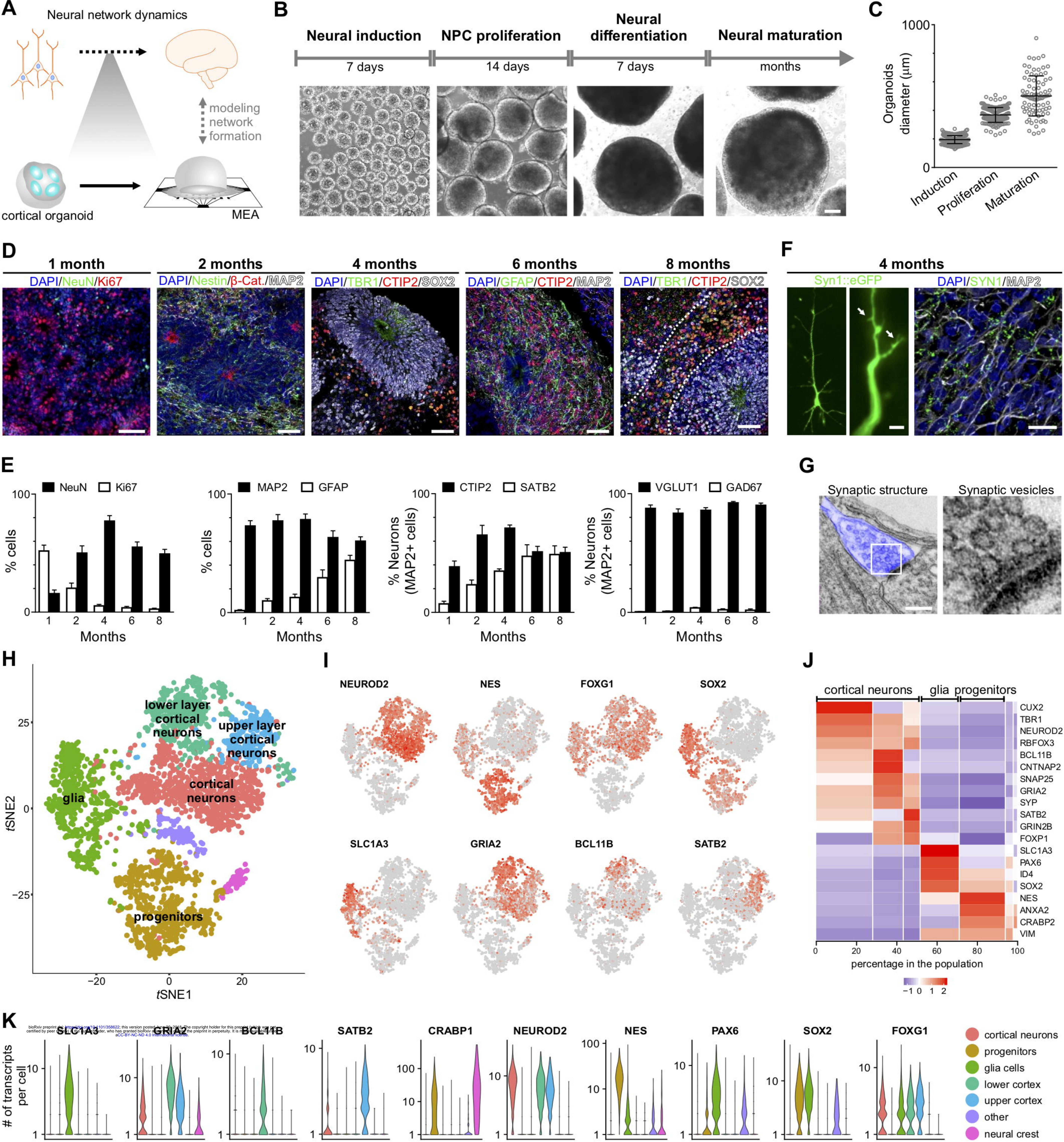
1073

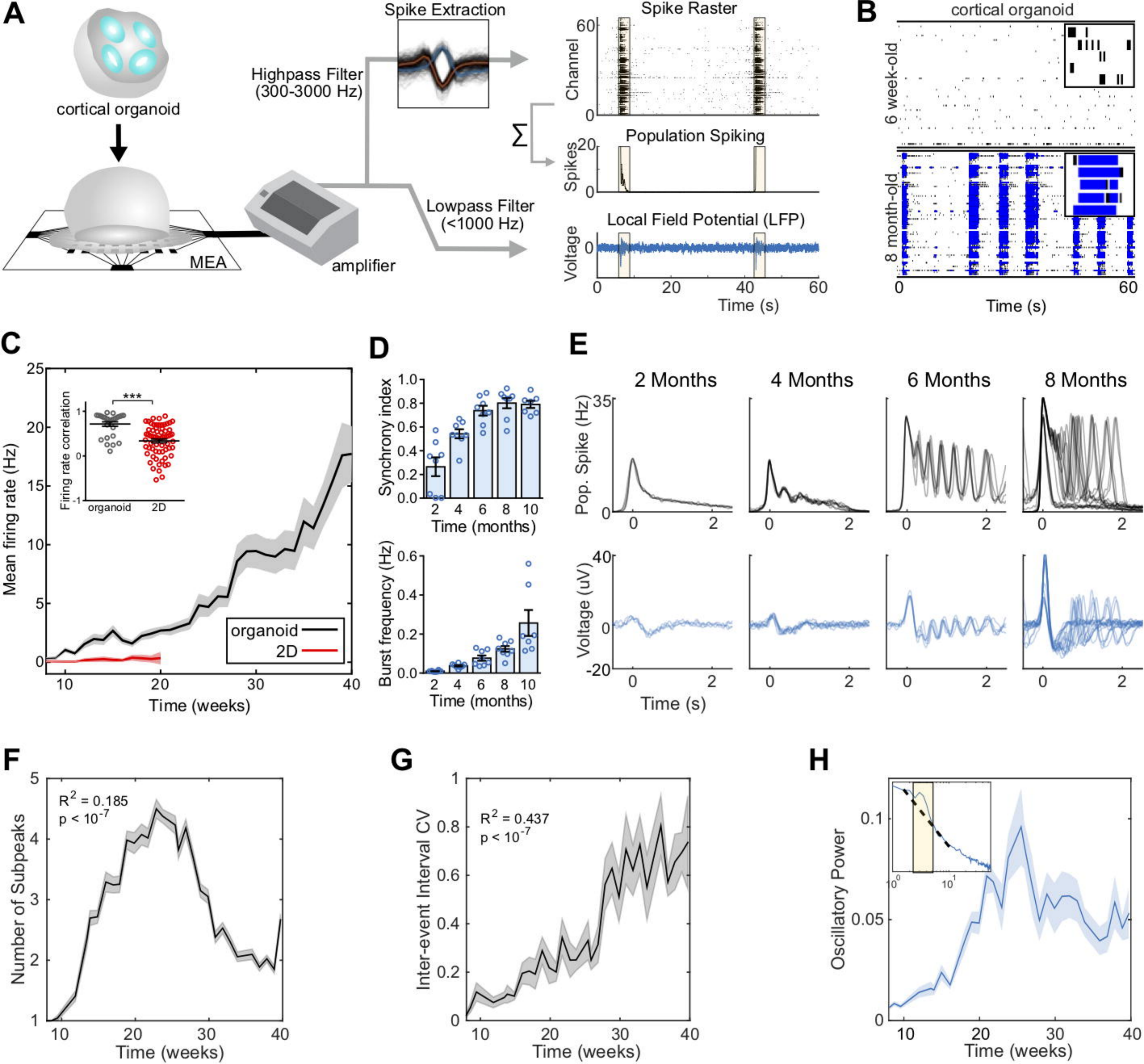
1074 **Supplementary Table 2. Electrophysiological features in preterm neonatal EEG dataset and**
 1075 **analogous features computed in organoid LFP.**

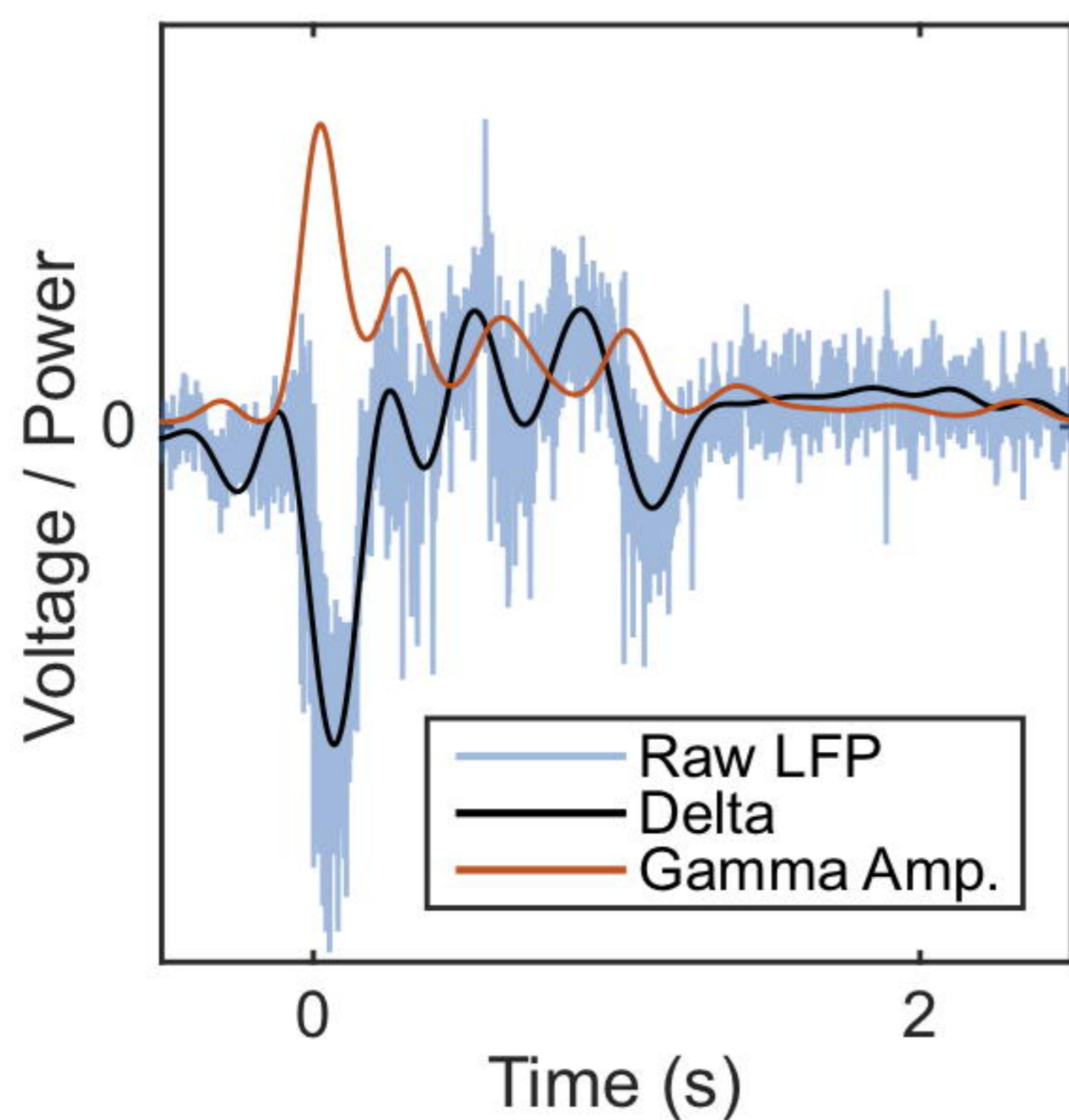
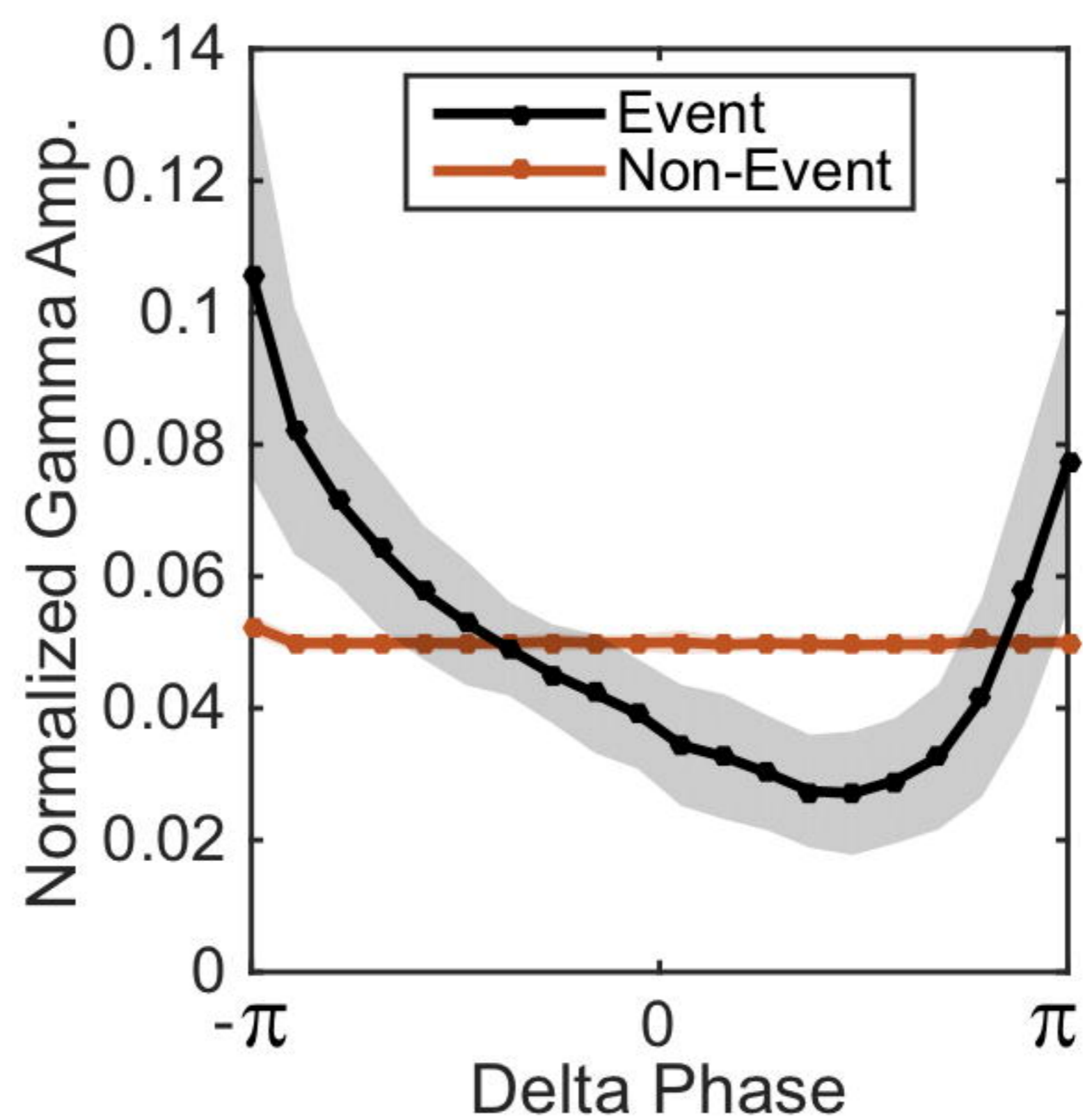
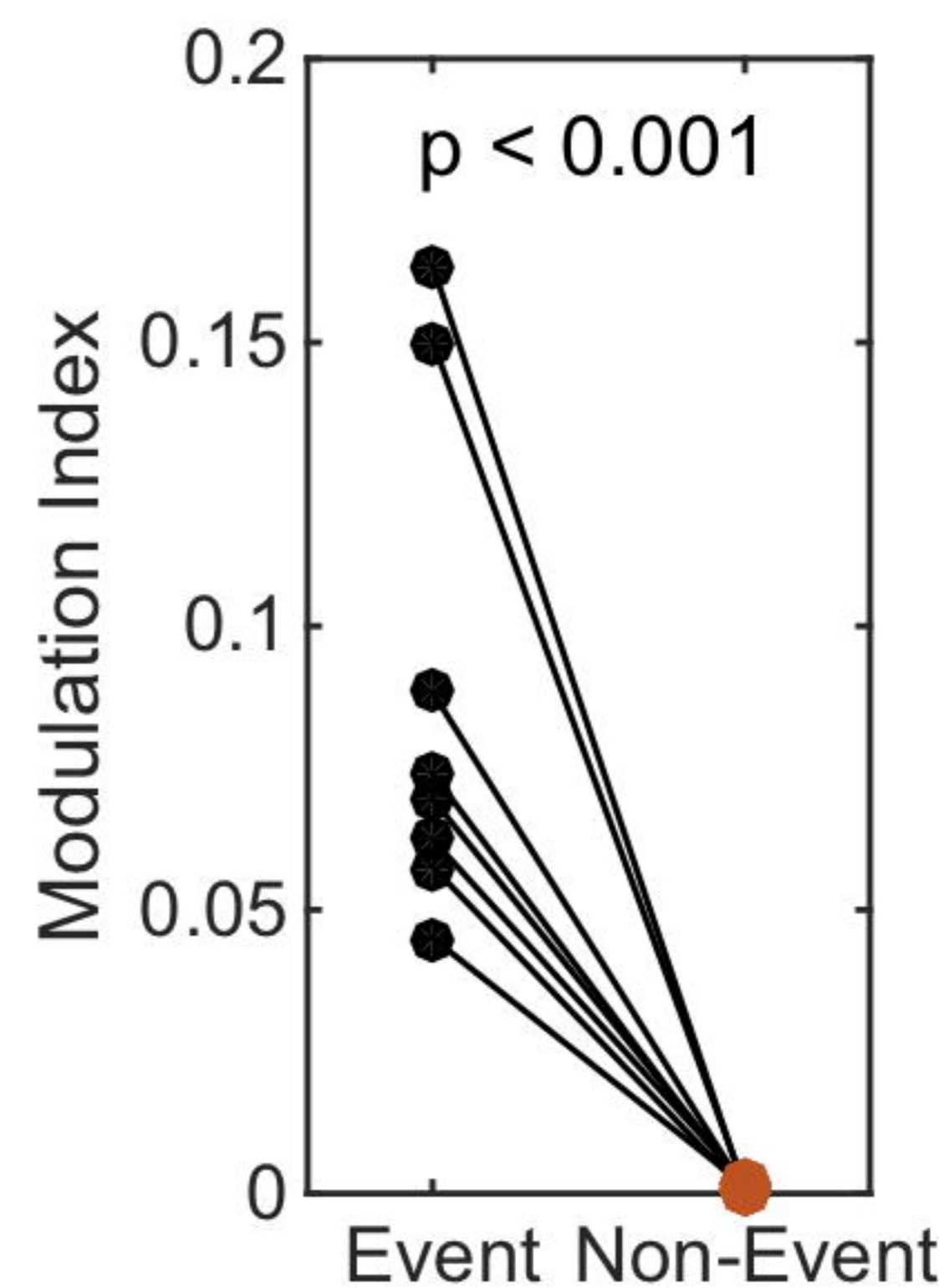
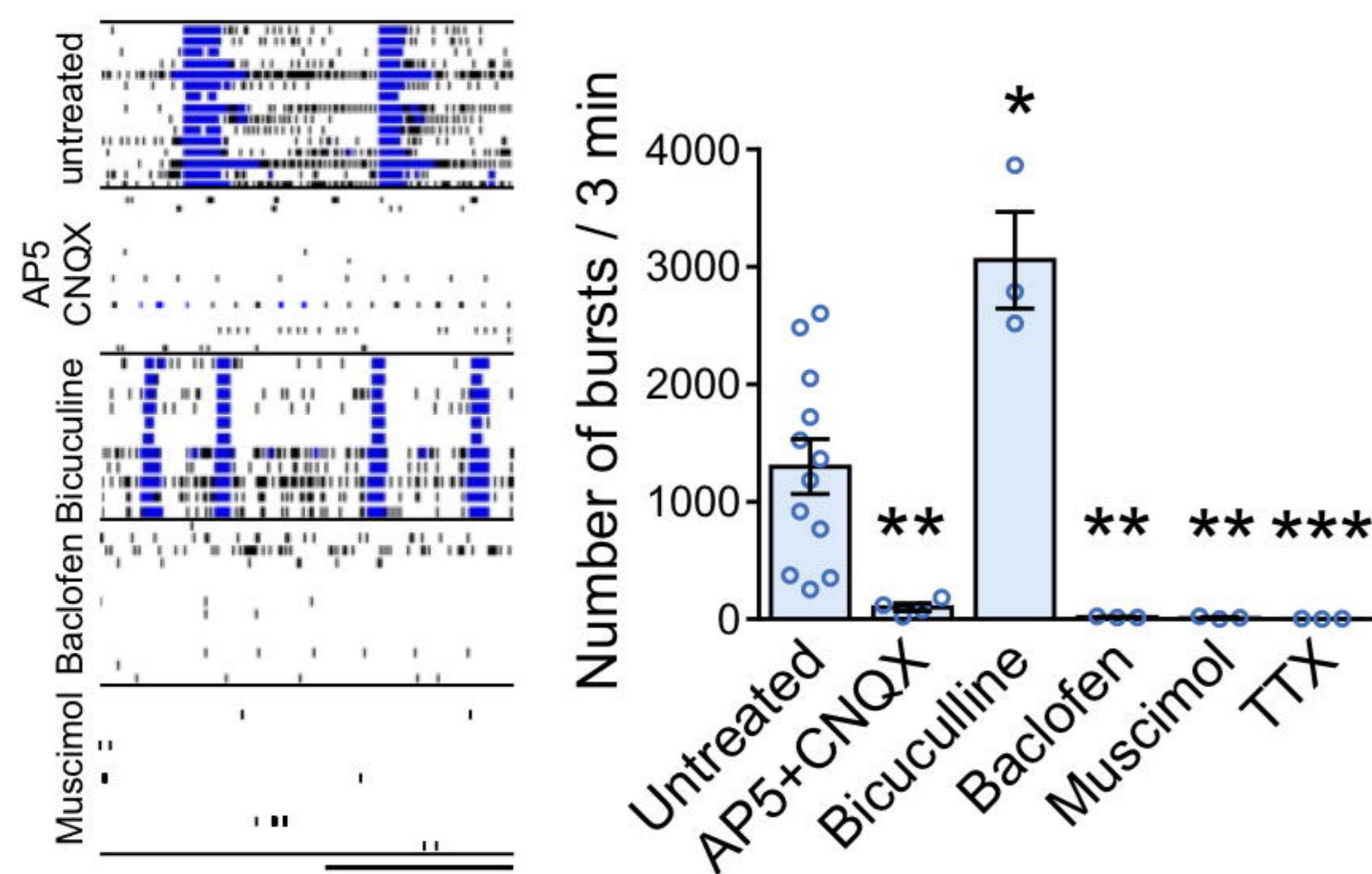
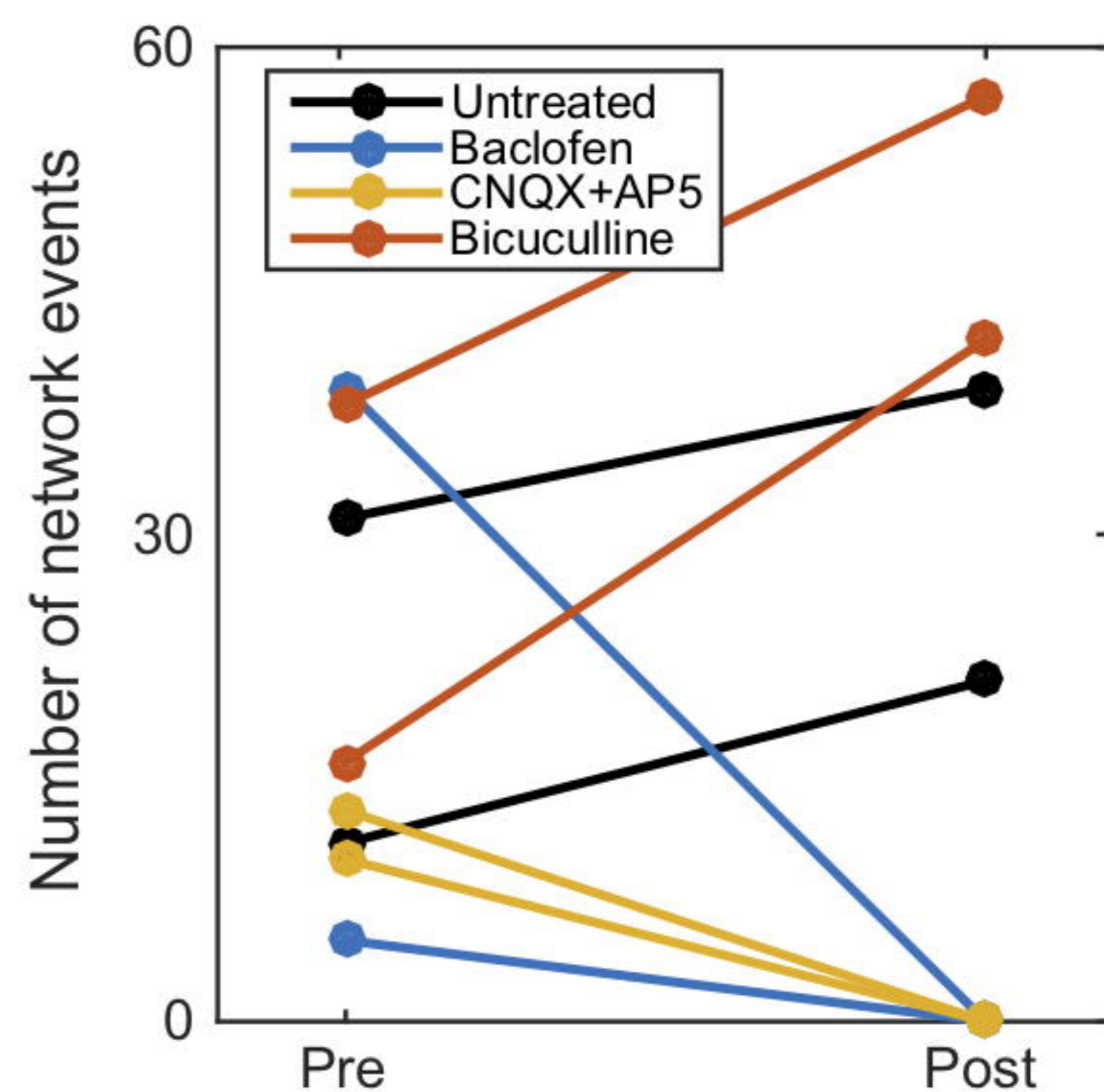
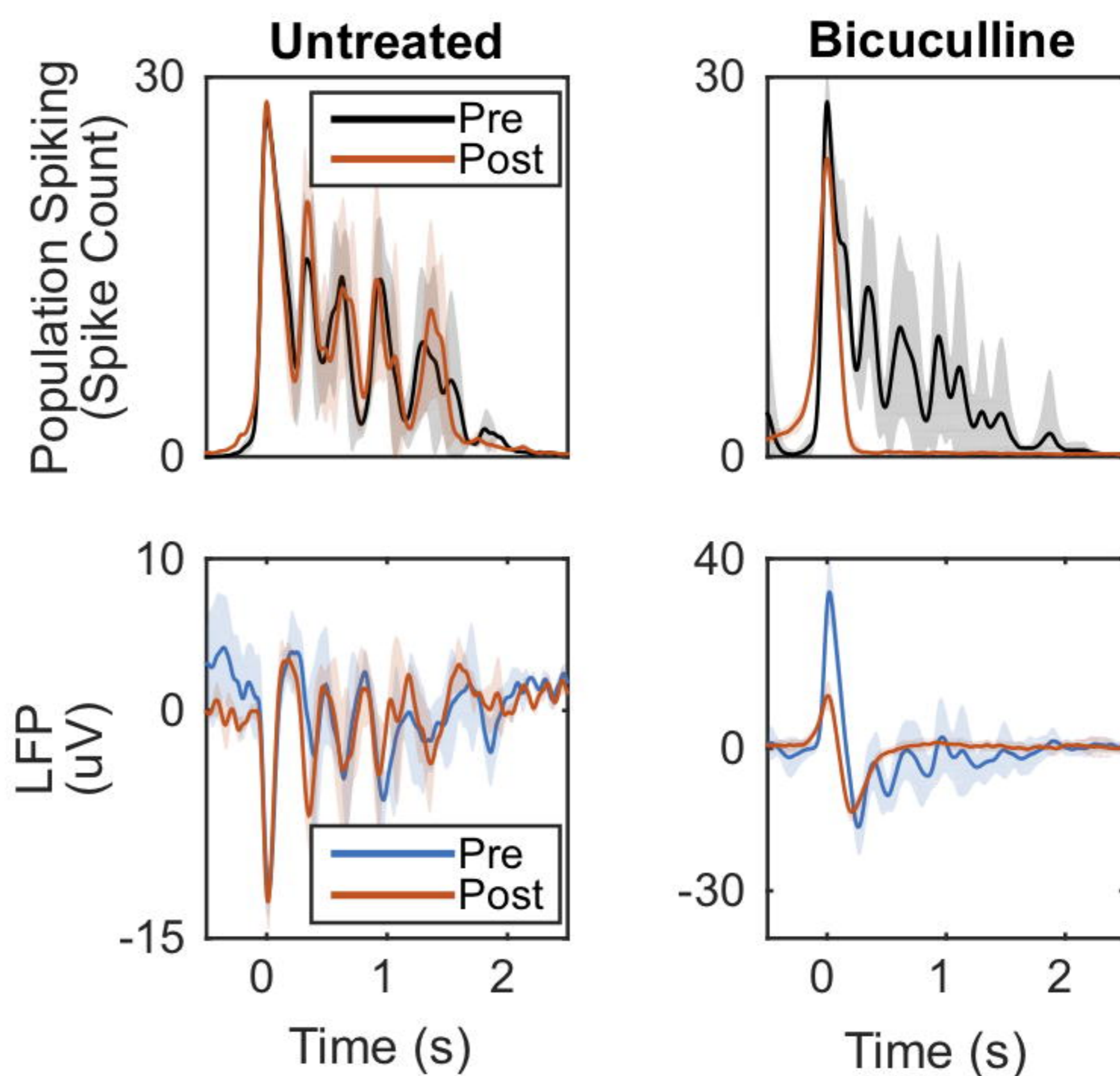
Neonatal EEG features	Computed organoid LFP features
Envelope (50%)	None
Envelope (5%)	None
Envelope (95%)	None
rEEG (50%)	None
rEEG (5%)	None
rEEG (95%)	None
SATs per hour	Network Events per hour
RMS SAT duration	RMS network event duration
SAT duration (50%)	Network event duration (50%)
SAT duration (5%)	Network event duration (5%)
SAT duration (95%)	Network event duration (95%)
RMS Inter-SAT Duration	RMS Inter-event Duration
Inter-SAT duration (50%)	Inter-event duration (50%)
Inter-SAT duration (5%)	Inter-event duration (5%)
Inter-SAT duration (95%)	Inter-event duration (95%)
Temporal Theta Power	None
Activation Synchrony Index	None
Interhemispheric Correlation	None
Total Spectral Power	None
Relative Delta Power	Relative Delta Power
Relative Theta Power	Relative Theta Power
Relative Alpha Power	Relative Alpha Power
Relative Beta Power	Relative Beta Power

1076 Shaded cells indicate features used in the age-prediction model.

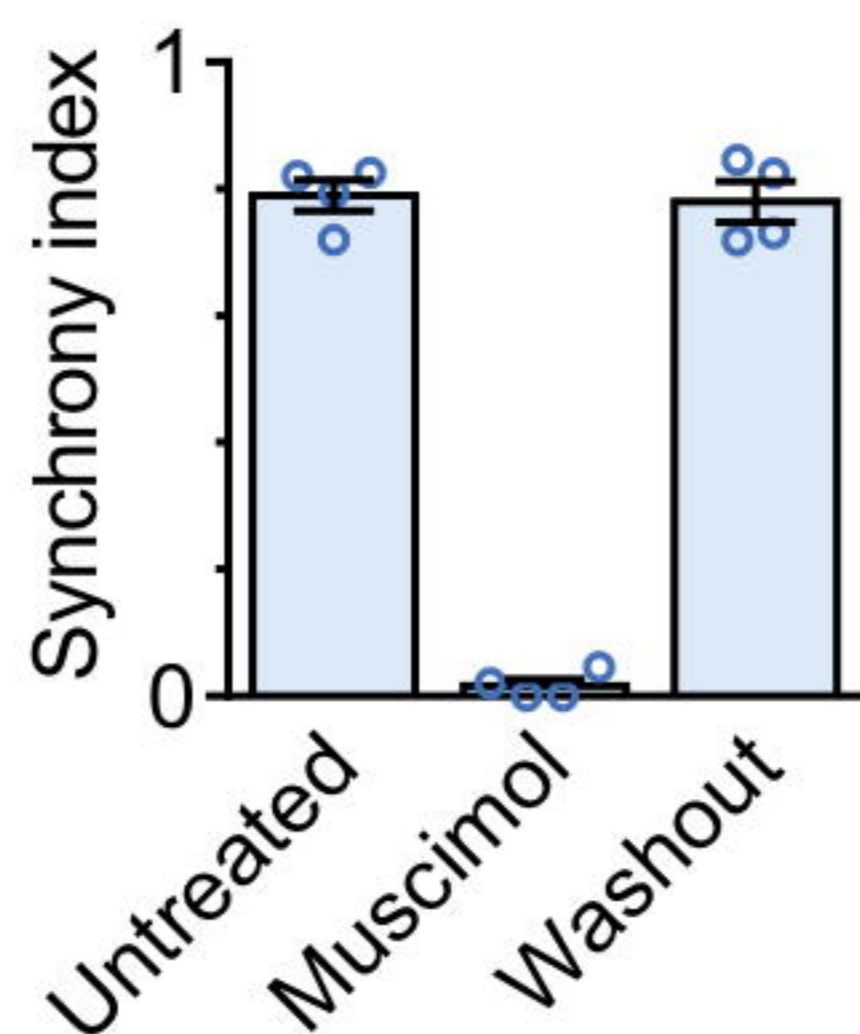
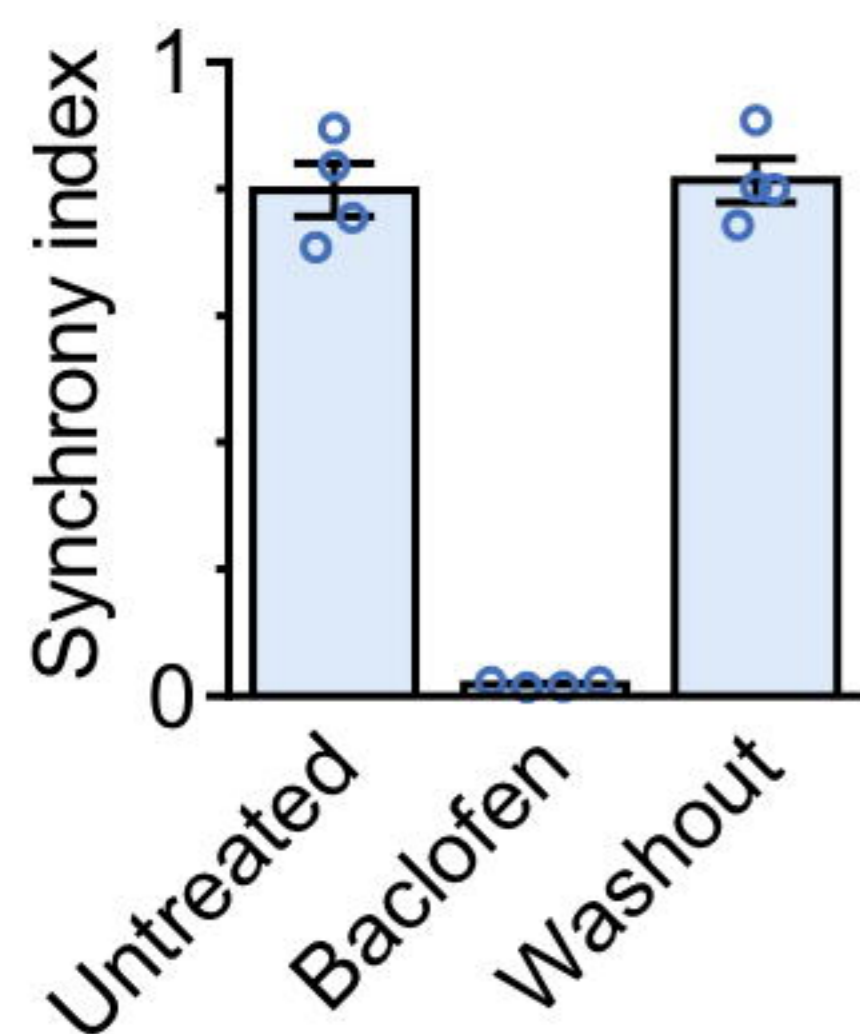
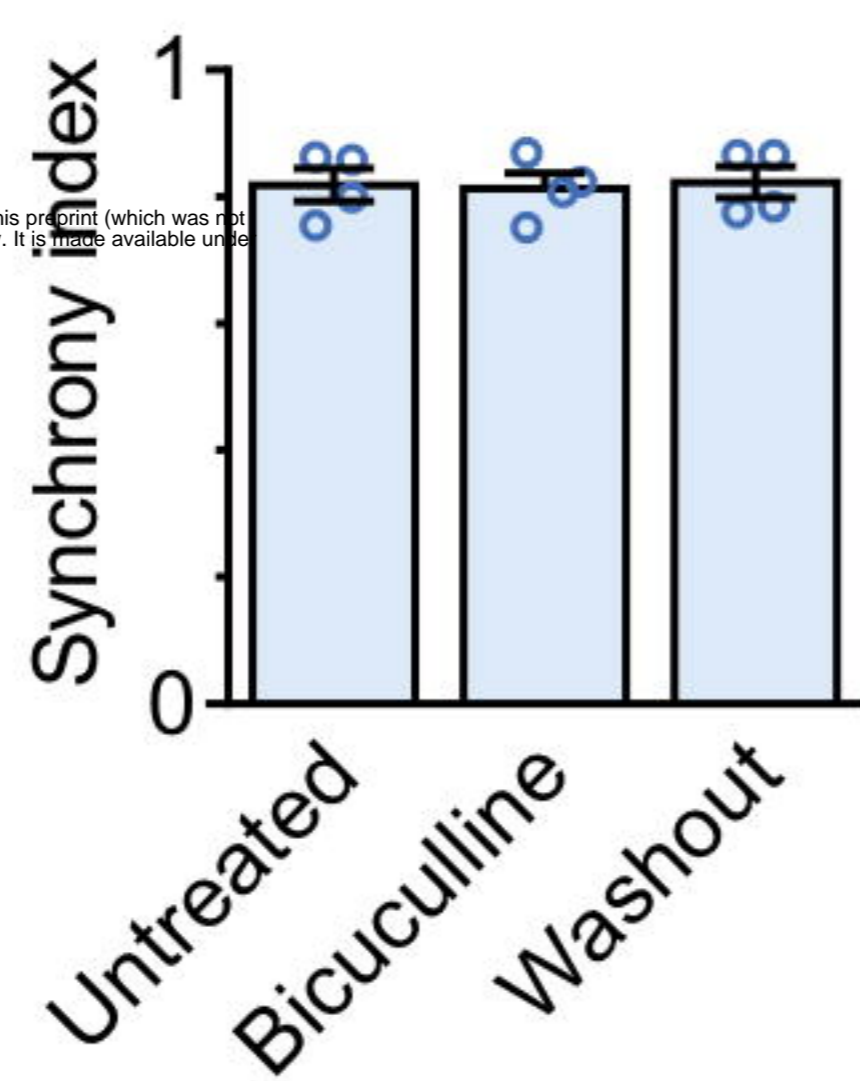
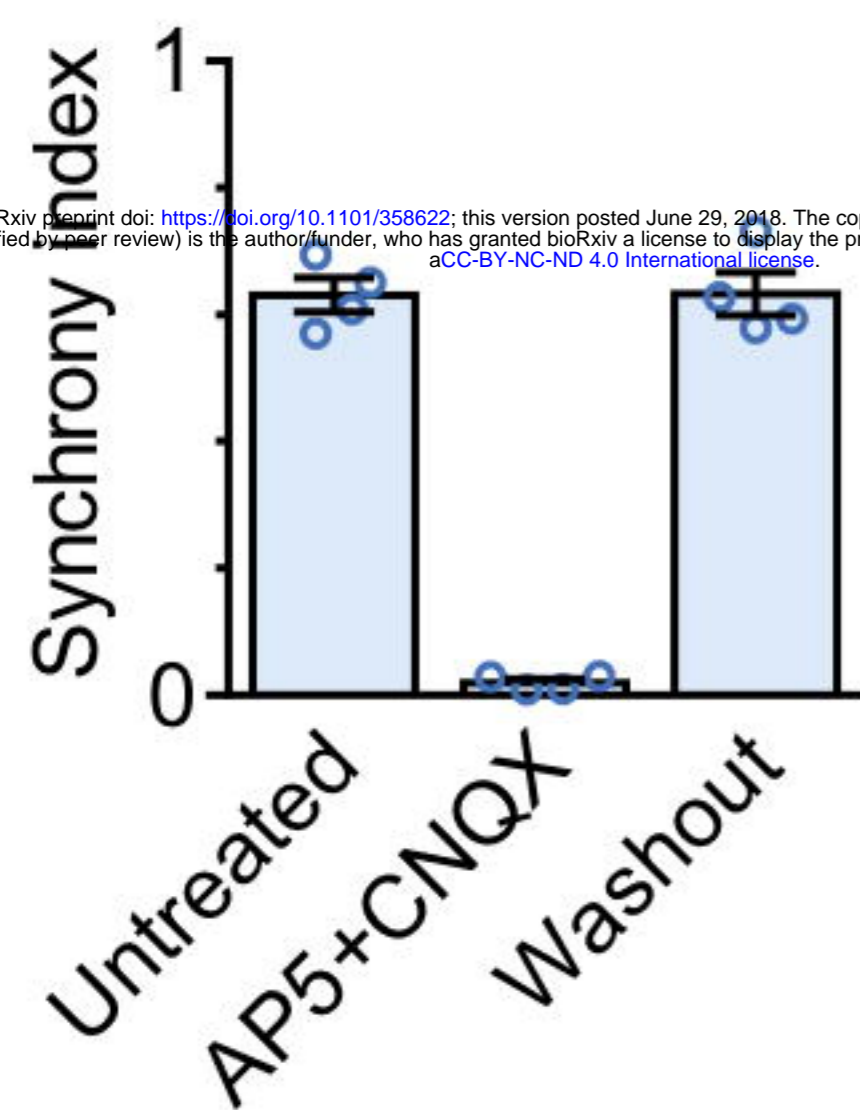
1077

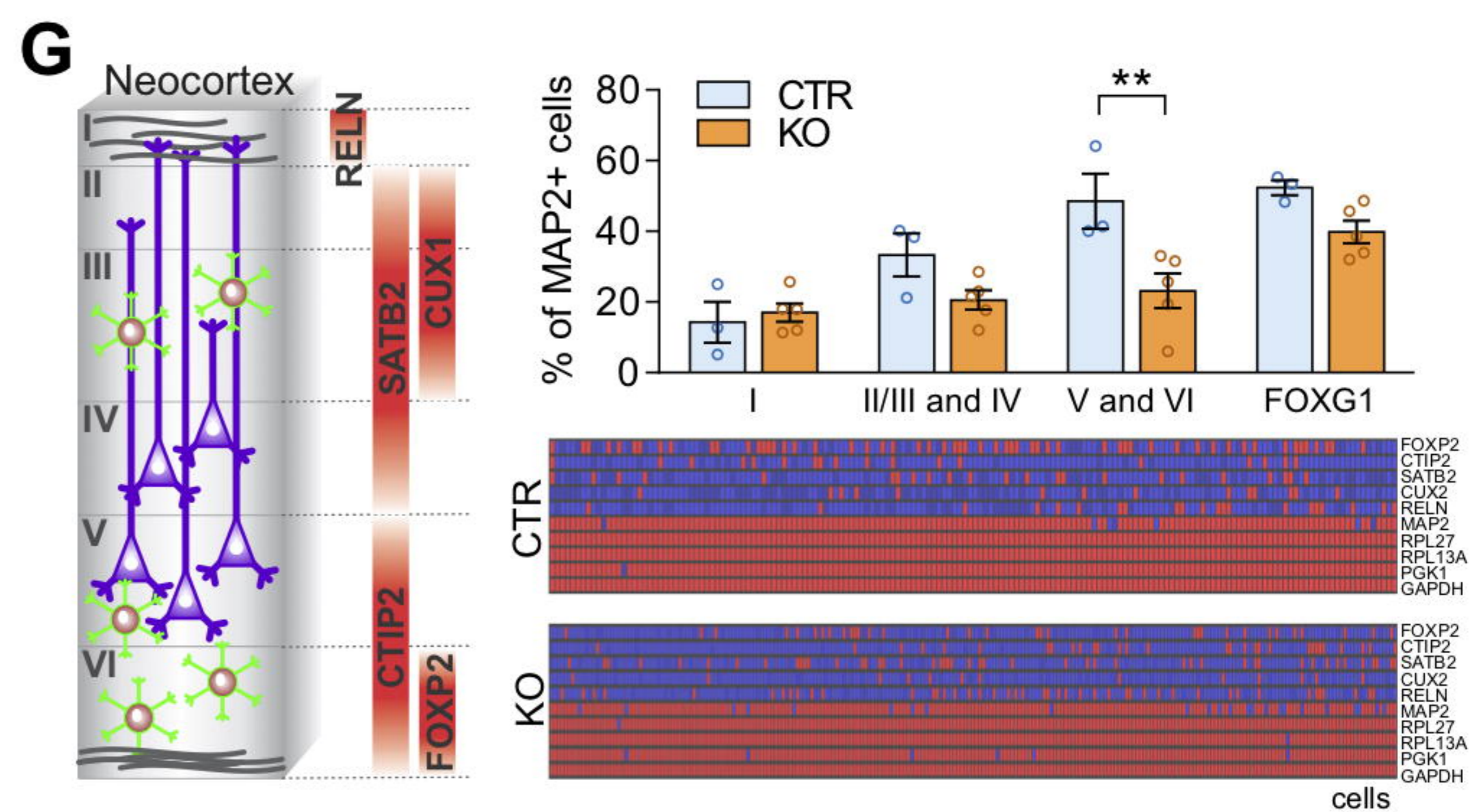
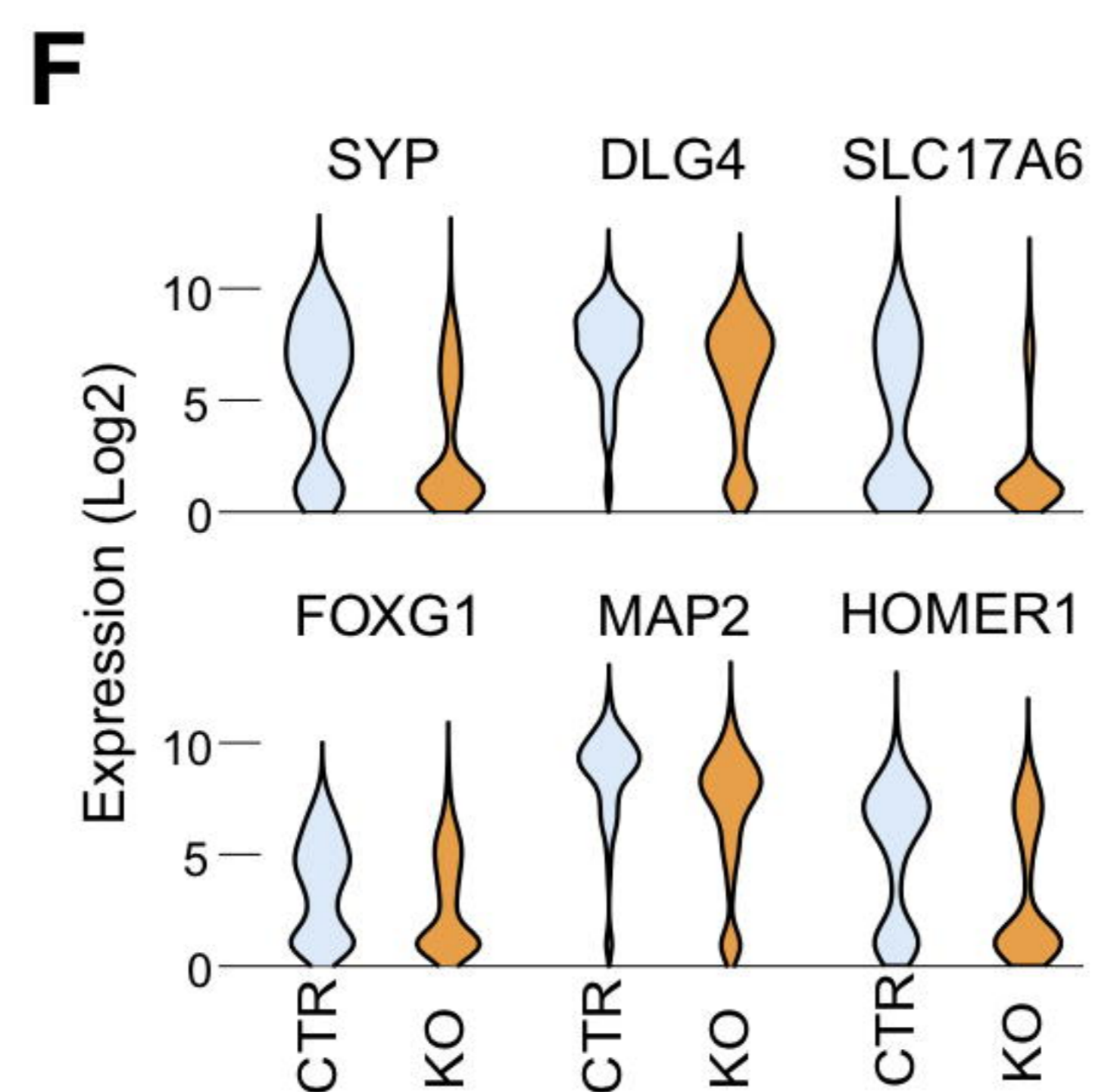
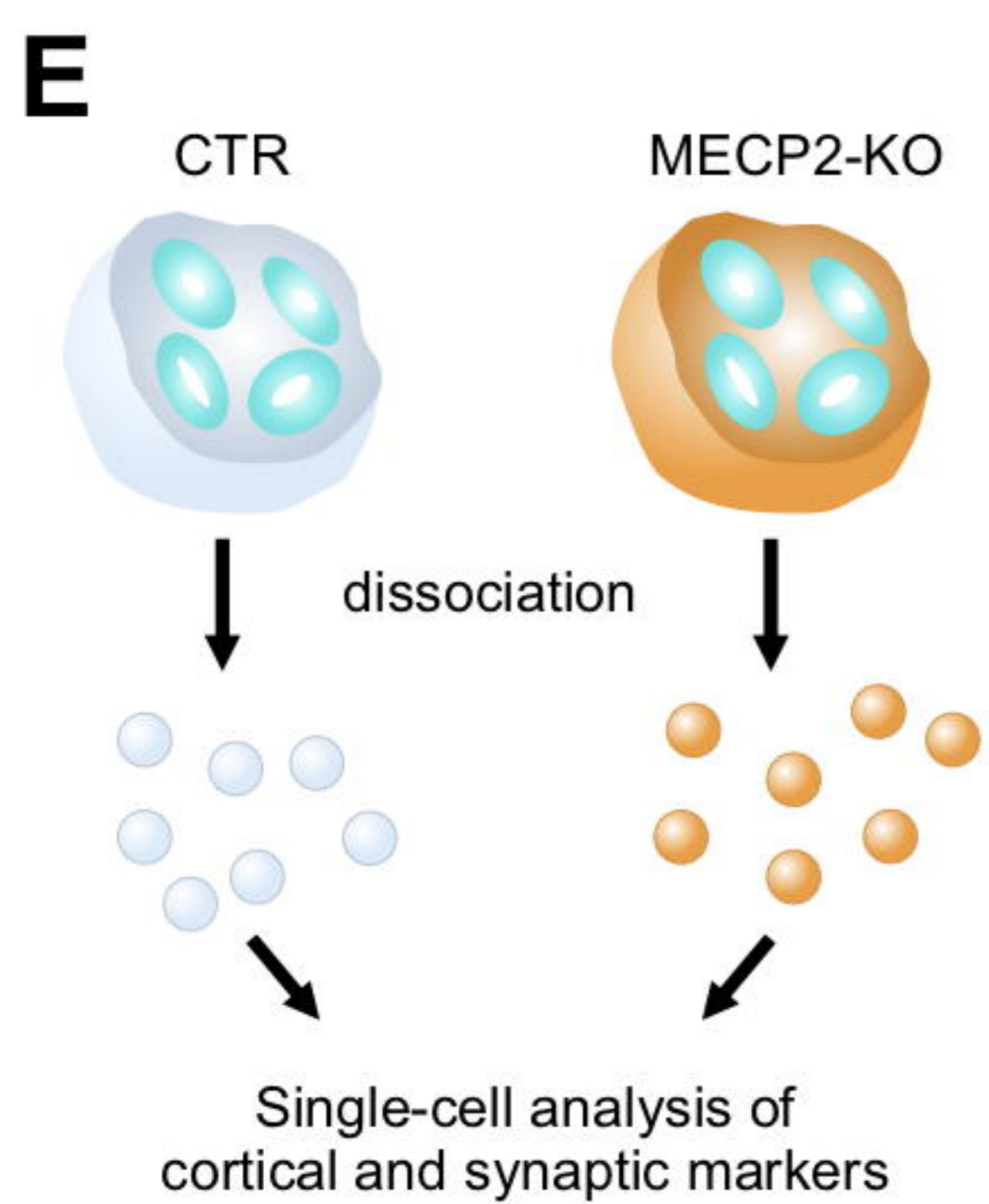
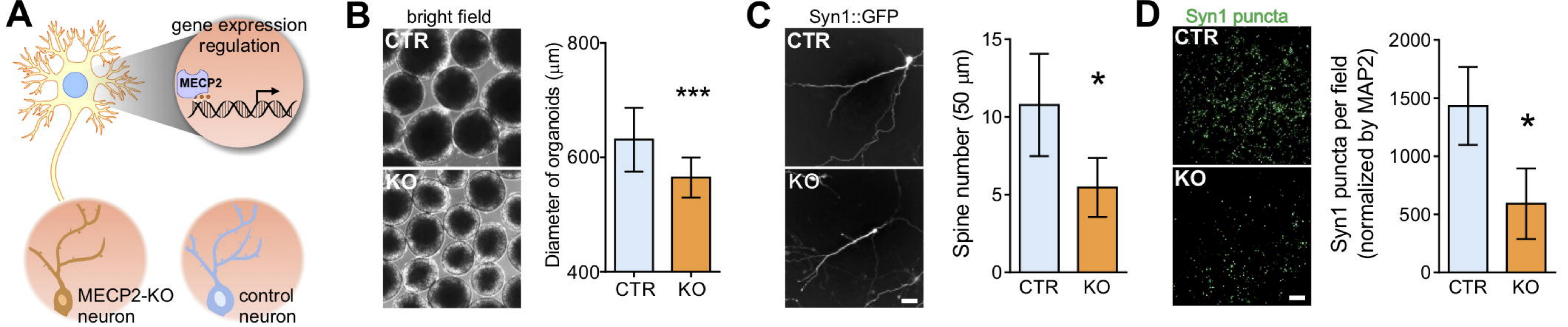




A**B****C****D****E****F**

bioRxiv preprint doi: <https://doi.org/10.1101/358622>; this version posted June 29, 2018. The copyright holder for this preprint (which was not certified by peer review) is the author/funder, who has granted bioRxiv a license to display the preprint in perpetuity. It is made available under aCC-BY-NC-ND 4.0 International license.





H bioRxiv preprint doi: <https://doi.org/10.1101/358622>; this version posted June 29, 2018. The copyright holder for this preprint (which was not certified by peer review) is the author/funder, who has granted bioRxiv a license to display the preprint in perpetuity. It is made available under aCC-BY-NC-ND 4.0 International license.

